Extreme Glacier Melt on~~in~~ the Central Tibetan Plateau during the Summer of 2022: Detection and Mechanisms

Fei Zhu[1,2], Meilin Zhu[3]*, Lu An[1,2]

[1]College of Surveying and Geo-Informatics, Tongji University, Shanghai, 200092, China.

[2]Center for Spatial Information Science and Sustainable Development, Tongji University, Shanghai, 200092, China.

[3]Center for the Pan-Third Pole Environment, Lanzhou University, Lanzhou 730000, China.

Corresponding author: Meilin Zhu* (zhuml@lzu.edu.cn)

Abstracts

Extreme glacier melt events accelerate mass loss, increase glacier instability, and temporarily mitigate downstream drought. However, the glacier energy-mass balance in the Geladandong region—the headwater of both the Yangtze River (China's longest river) and Siling Co (Tibet's largest lake)—and its connection to the unprecedented 2022 summer melt remain insufficiently quantified. ~~To address this gap, we integrated in situ mass balance observations (October 2019–July 2022) and glacio-meteorological data from a 5,700 m monitoring site (October 2020–July 2022) with a surface energy-mass balance model, and applied a novel dual-threshold framework (based on mean and standard deviation) to identify extreme mass loss/melt events in short-term glacier mass balance records. Our novel methodology identified 2021–2022 as a period of extreme mass loss and melt intensity, with melt during the 2022 summer heatwave reaching unprecedented extremes. Over 52 days, the heatwave generated 1,135 mm w.e. of melt—accounting for 65.2% of the total 2021–2022 melt, equivalent to 1.8 and 2.3 times the melt recorded in 2019–2020 and 2020–2021, respectively. This extreme melt was driven by energy balance anomalies over glacier surface, including reduced albedo, increased incoming longwave radiation, and enhanced sensible heat fluxes, with these processes strongly linked to persistent high temperatures and diminished precipitation. Such anomalies in the energy balance were driven by large-scale atmospheric circulation anomalies—specifically, the concurrent intensification and westward expansion of the Western Pacific Subtropical High (WPSH) and the eastward extension of the South Asian High (SAH). This study establishes a novel framework for identifying extreme mass loss events and substantially advances understanding of glacier mass balance responses to extreme weather and climate events.~~ To address this gap, we integrated in situ mass balance observations and glacio-meteorological data from a 5,700 m monitoring site with an energy-mass balance model and applied a novel dual-threshold framework (based on mean and standard deviation) to identify extreme mass loss/melt events in short-term glacier mass balance records. Our novel methodology identified 2021–2022 as a

period of extreme mass loss and melt intensity, with melt during the 2022 summer heatwave reaching unprecedented extremes. These heatwaves caused an increase in melt amount of 317.8 mm w.e., amounting to 1.66 and 1.69 times the values recorded for the same period in 2019/20 and 2020/21, respectively. This extreme melt was driven by energy balance anomalies over the glacier surface, including reduced albedo, increased incoming longwave radiation, and enhanced sensible heat fluxes, processes that were strongly linked to persistent high temperatures. Such anomalies were driven by large-scale atmospheric circulation patterns, specifically the concurrent intensification and westward expansion of the Western Pacific Subtropical High, the eastward extension of the South Asian High, and the northward shift of the westerly circulation. This study proposes a framework for identifying extreme mass loss events in short-term glacier mass balance records and provides insights into glacier mass balance responses to extreme weather and climate events.

Keywords: Energy and mass balance, Extreme heat waves, Extreme melt, Extreme mass loss

1. Introduction

~~Extreme glacier melt events directly reflect glacier mass balance responses to extreme weather and climate events, such as heatwaves, droughts, and wildfires. Given the increasing frequency of extreme glacier mass loss events across Tibetan Plateau (TP) and surrounding regions since the early 21st century, this short-term intensive depletion events significantly alter long-term glacier mass balance trends and increase risks of glacier-related geohazards (Yao et al., 2022; Immerzeel et al., 2020; You et al., 2020; Zhang et al., 2023b; Zhu et al., 2024b). In recent decades, scientific focus has increased on understanding spatiotemporal patterns and driving mechanisms of glacial retreat and thinning across TP (Bolch et al., 2012; Yao et al., 2012; Brun et al., 2017; Hugonnet et al., 2021).~~ Extreme glacier melt events directly reflect glacier mass balance responses to extreme weather and climate events, such as heatwaves, droughts (Zhu et al., 2024a; Xu et al., 2024; Zhu et al., 2026b; Van Tiel et

al., 2026). Across the Tibetan Plateau and surrounding regions, evidence from Xiao Dongkemadi Glacier, which holds the longest mass balance record in the central Tibetan Plateau (TP) with observations since 1989, indicates that extreme mass loss events have been concentrated in 2000–2022, compared to 1989–2000 (Yao et al., 2012; Zhu et al., 2026a). In recent decades, scientific focus has increased on understanding spatiotemporal patterns and driving mechanisms of glacial retreat and thinning across TP (Bolch et al., 2012; Yao et al., 2012; Brun et al., 2017; Hugonnet et al., 2021). Studies have systematically revealed how atmospheric circulation patterns and dominant climate variables govern spatiotemporal variations in glacier mass balance across TP. Large-scale atmospheric anomalies generate distinct regional disparities in air temperature-precipitation regimes, potentially explaining the observed spatial heterogeneities in glacier mass balance (Yao et al., 2012). Meteorological controls exhibit strong regional differences: annual precipitation dominates mass balance variability in northwestern TP glaciers, whereas ablation-season air temperatures primarily regulate mass balance in southeastern regions (Zhu et al., 2018, 2020, 2021). Monsoon-driven cloud cover significantly influences summer surface energy budgets, as evidenced by detailed observations at East Rongbuk Glacier on the northern slopes of Mount Everest (Liu et al., 2021). These findings collectively demonstrate pronounced spatial heterogeneity in the sensitivity of TP glaciers to climate forcing. However, understanding the mechanisms underlying extreme mass loss events across TP and adjacent regions remains inadequate.

Emerging evidence identifies compound heat-drought events as primary drivers of extreme glacier mass loss. Regional case studies across cryosphere hotspots—including the eastern Tien Shan (Xu et al., 2024), Qilian Mountains (Chen et al., 2024), and Tanggula and Nyainqêntanglha ranges (Zhu et al., 2024b)—reveal unprecedented mass loss rates associated with atmospheric teleconnections and glacier surface energy budget anomalies. These events typically result from synergistic interactions between external forcing (heat extremes/precipitation deficits) and intrinsic glacier responses (albedo feedbacks/turbulent heat flux anomalies).

When superimposed, these drivers can push glacier systems beyond equilibrium thresholds within weeks, producing nonlinear mass losses that challenge conventional model predictions. However, comprehensive event attribution remains challenging across most of TP.

~~This knowledge gap stems from two critical limitations: (1) methodological constraints in detecting extremes from short mass balance records (under ten years), and (2) sparse in situ monitoring networks—fewer than ten TP glaciers have decadal-scale measurements. Traditional extreme detection methods (e.g., 10th percentile thresholds, generalized extreme value [GEV] distributions) require multi-decadal data unavailable for over 90% of TP glaciers. Consequently, developing robust frameworks for identifying extremes in short-term observations (under ten years) is essential for the region.~~

This knowledge gap stems from two critical limitations: (1) methodological constraints in detecting extremes from short mass balance records (under ten years), and (2) sparse in situ monitoring networks—fewer than ten TP glaciers have decadal-scale measurements. Traditional extreme detection methods (e.g., 10th percentile thresholds, generalized extreme value distributions) require multi-decadal data unavailable for over 90% of TP glaciers. Consequently, developing and testing frameworks, such as the dual-threshold approach proposed in this study, for identifying extremes from short-term observations (under ten years) are essential for advancing glacier research in this region.

The exceptional 2022 heatwave, characterized by unprecedented air temperature anomalies and precipitation deficits, served as an ideal natural experiment to address these challenges. Researchers have systematically analyzed the temporal characteristics (frequency/duration), intensity metrics, and hydrological impacts of the 2022 heatwave-drought events in both the Yangtze River Basin (Hua et al., 2023; Jeong et al., 2023) and TP (Yan et al., 2024; Zhou et al., 2024). Hua et al. (2023) demonstrated that a 6.45 °C temperature anomaly, observed in central China over the 21-day period from 6 to 26 August 2022, broke historical records and established a

new threshold for defining future record-breaking daily maximum temperatures in the region. ~~Hua et al. (2023) demonstrated that a 6.45 °C temperature anomaly in central China broke historical records and reshaped climatological baselines for extreme temperature projections.~~ During summer 2022, central-eastern TP recorded mean maximum air temperatures 3.5 °C above the 1961–2013 baseline (Zhou et al., 2024). Concurrently, central-eastern TP precipitation was 2.4 σ below the 1961–2013 mean (Zhou et al., 2024), while southern China experienced rainfall deficits of 2–3 $mm \cdot day^{-1}$ (Jeong et al., 2023). Multiple drivers have been identified, including synoptic-scale circulation anomalies (Hua et al., 2023; Duan et al., 2024), Indian Ocean Dipole–La Niña interactions (Jeong et al., 2023), land-atmosphere feedbacks (Li et al., 2023), and localized energy budget perturbations (Tian et al., 2023; Zhang et al., 2023b). These studies collectively reveal that both TP and eastern China faced unprecedented extreme heat and precipitation deficits during summer 2022.

The key glaciated complexes most exposed to this extreme event—located in the Central Tanggula Mountains (encompassing the Geladandong and Dongkemadi regions, and Puruogangri Ice Cap), a critical cryospheric zone in central TP—provide a unique opportunity to develop novel methodologies for identifying extreme mass loss events and elucidating their driving mechanisms. Continuous mass balance monitoring began in 1989 at Xiao Dongkemadi Glacier in the Dongkemadi region (Pu et al., 2008; Yao et al., 2012). Since entering a negative mass balance regime around 1995, Xiao Dongkemadi Glacier has experienced accelerated mass loss at ~−0.3 m w.e. yr^{-1} since 2000 (Pu et al., 2008; Yao et al., 2012; Kang et al., 2015). Research demonstrates that summer mass balance controls annual mass balance variations in summer-accumulation-type glaciers in the Dongkemadi region (Liang et al., 2018). The Geladandong region recorded glacier mass loss rates of -0.24 ± 0.08 m w.e. yr^{-1} from the 1960s to 2018 (King et al., 2023). Sangqu Glacier, located south of Geladandong, was selected for in situ glacio-meteorological observations. Meltwater from Sangqu Glacier drains into Siling Co, the largest lake in Tibet. Therefore, investigating extreme mass loss events in this region will improve the understanding

of glacier change patterns and support sustainable water resource management.

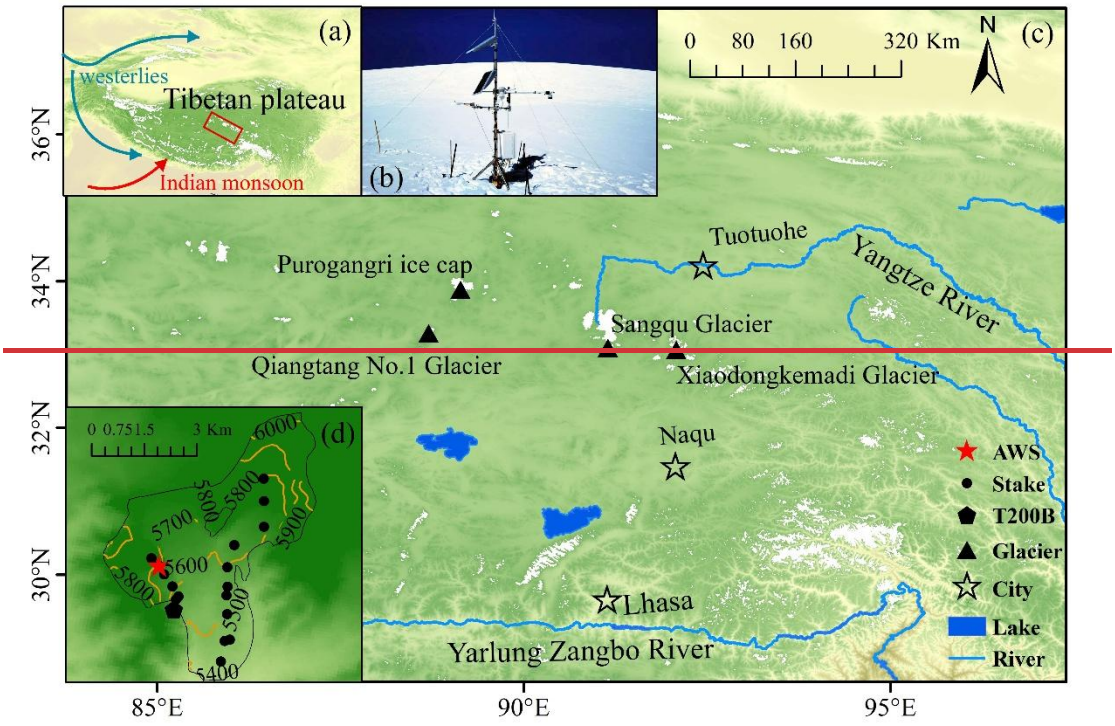
Hence, this study aims to (i) investigate the energy-mass balance characteristics of Sangqu Glacier in the Geladandong region; (ii) develop a novel framework for detecting extreme mass loss events in short-term glacier mass balance records; and (iii) elucidate melting mechanisms driven by the unprecedented 2022 summer heatwaves. By integrating multi-source observational data with a surface energy-mass balance model, this work advances understanding of glacier responses to extreme heatwaves and proposes an innovative thermal-threshold framework—a methodological advancement addressing critical gaps in TP cryosphere research.

2. Study Area

~~The valley-type continental Sangqu Glacier (33.1951°N, 91.1362°E) in Geladandong was selected as the study site (Figure. 1). This south-facing glacier has a length of 2.2 km and covers 18 km². Spanning an elevational range of 5,400–6,104 m a.s.l., its equilibrium line altitude (ELA) is ~5,700 m a.s.l. (Guo et al., 2015). Situated in central TP, the region experiences low air temperatures and a semi-arid continental climate. Over 70% of annual precipitation occurs during June–September, coinciding with the warmest season (Zhu et al., 2024a). Glacier ablation and accumulation in Geladandong primarily occur from June to September, characterized by a short melt season (Pu et al., 2008). Multi-temporal digital elevation model (DEM) differencing and in situ stake measurements reveal continuous mass loss in this region since the 1990s (Yao et al., 2012; King et al., 2023). Moreover, Sangqu Glacier lies at the northern limit of Indian monsoon influence (Tian et al., 2001; Yao et al., 2013).~~

The valley-type continental Sangqu Glacier in Geladandong was selected as the study site (Fig. 1). This south-facing glacier has a length of 2.2 km and covers 18 km². Spanning an elevational range of 5,400–6,104 m a.s.l.. Situated in central TP, the region experiences low air temperatures and a semi-arid continental climate. Over 70% of annual precipitation occurs during June–September, coinciding with the warmest season (Zhu et al., 2024a). Glacier ablation and accumulation in Geladandong primarily occur from June to September, characterized by a short melt

season (Pu et al., 2008). Multi-temporal digital elevation model differencing and in situ stake measurements reveal continuous mass loss in this region since the 1990s (Yao et al., 2012; King et al., 2023). Based on the combined in situ and ERA5-corrected precipitation data, the mean annual precipitation at the Sangqu Glacier site was 510.5 mm for the period October 2019--September 2022. Geodetic mass balance estimates from Dussaillant et al. (2025) indicate that Sangqu Glacier lost ~515.4 mm w.e. yr^{-1} over the period 1957–2024, consistent with the regional mass loss pattern. Moreover, Sangqu Glacier lies at the northern limit of Indian monsoon influence (Tian et al., 2001; Yao et al., 2013). Based on the observed ice temperatures and the presence of meltwater percolation and refreezing in the ablation zone, Sangqu Glacier is polythermal, with cold ice in the upper accumulation zone and temperate ice in the ablation zone. This thermal regime is consistent with observations on neighboring glaciers in the central Tibetan Plateau, such as Xiao Dongkemadi Glacier, where superimposed ice formation plays a significant role in the mass balance (Fujita et al., 1996).



~~Figure 1. Overview of the study area. (a) and (c) Location of the study area on TP. (b) Photos of AWS on Sangqu Glacier (Photo credit: Fei Zhu). (d) Stakes in October 2019, automatic weather stations, and precipitation gauges are located on Sangqu Glacier.~~

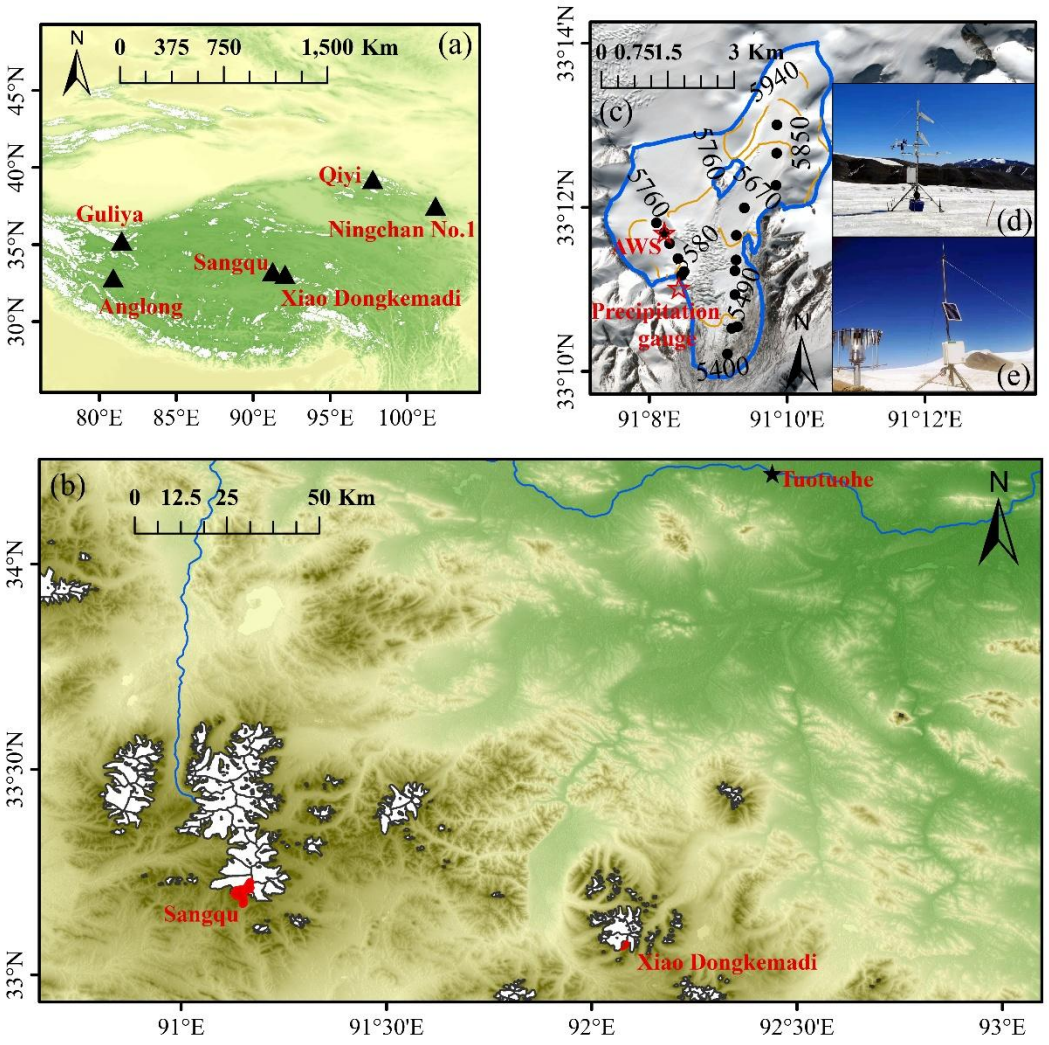


Figure 1. Overview of the study area. (a, b) Geographical location of the glacier on the Tibetan Plateau: (a) regional context; (b) enlarged local map. (c) Sentinel-2 image (2022-12-05) with contour lines showing the topography of Sangqu Glacier. (d, e) Photographs of the AWS and the precipitation gauge on Sangqu Glacier (Photo credit: Fei Zhu). The positions of the AWS, precipitation gauge, and stakes are indicated in panel (c).

3. Data

3.1 Meteorological Data on Glacier Surface

~~An automatic weather station (AWS) was installed on Sangqu Glacier at 5,700 m a.s.l. in October 2020 (Figure. 1b and 1d). Hourly measurements included air temperature, relative humidity, wind speed, incoming/outgoing shortwave radiation,~~

~~and incoming/outgoing longwave radiation. Air temperature and relative humidity probes, along with wind speed, were mounted 2 m above the glacier surface. Radiation sensors were installed greater than 1.6 m above the surface. Data from July 2021 were incomplete due to power failure; operations resumed on 13 July 2021. A Geonor T-200B precipitation gauge on adjacent bedrock (5,665 m a.s.l.) recorded precipitation at 30-min intervals (Figure. 1d). Meteorological data cover the period October 2020 to July 2022.~~

An automatic weather station (AWS) was installed on Sangqu Glacier at 5,700 m a.s.l. in October 2020 (Fig. 1c and 1d). Hourly measurements included air temperature, relative humidity, wind speed, incoming/outgoing shortwave radiation, and incoming/outgoing longwave radiation. Air temperature and relative humidity probes, along with wind speed, were mounted 2 m above the glacier surface. Radiation sensors were installed more than 1.6 m above the surface. Data from July 2021 were incomplete due to power failure; operations resumed on 13 July 2021. A Geonor T-200B precipitation gauge, equipped with a double-alter shield to minimize wind-induced undercatch, was installed on adjacent bedrock (5,665 m a.s.l.) to record precipitation at 30-min intervals (Fig. 1e). Meteorological data cover the period October 2020 to July 2022. As the observational data only cover the period up to July 2022, the meteorological forcing for August–September 2022 was reconstructed using ERA5 reanalysis data (see Sect. 4.1).

3.2 Glacier Mass Balance Data

Glacier mass balance measurements began in October 2019 using stake and snow-pit methods. Stakes were distributed between 5,400 and 5,750 m a.s.l. (Fig. 1c). ~~Glacier mass balance measurements began in October 2019 using stake and snow-pit methods. Stakes were distributed between 5,400 and 5,750 m a.s.l.. S~~take heights and snow-pit characteristics were measured in October 2019, October 2020, October 2021, and July 2022. Using these measurements and assumed densities (snow: 300 kg m^{-3}; ice: 900 kg m^{-3}), mass balance data were derived for three periods: October 2019–October 2020, October 2020–October 2021, and October 2021–July 2022. Point

and glacier-wide mass balances were calculated following Yao et al. (2012).

3.3 Other Data

Hourly ERA5 reanalysis data (Hoffmann et al., 2019), including air temperature, precipitation, relative humidity, wind speed, and incoming shortwave radiation, were used. Additionally, variables at the 500, 200, and 300 hPa pressure levels, including geopotential height, horizontal wind, temperature, and specific humidity, were also employed in this study. This data was used to reconstruct meteorological conditions at the AWS locations and to analyze the characteristics and underlying causes of the extreme melt.~~Hourly ERA5 reanalysis data (Hoffmann et al., 2019) including air temperature, precipitation, relative humidity, wind speed, and incoming shortwave radiation were used. These data reconstructed meteorological conditions at the AWS locations.~~ Glacier boundaries were obtained from the Second Chinese Glacier Inventory (Guo et al., 2015). The 90-m resolution Shuttle Radar Topography Mission (SRTM) digital elevation model (DEM) was used to extract elevation, slope, and aspect. These data also drove model calculations of top-of-atmosphere radiation (Hock and Holmgren, 2005).

4. Methods

4.1 Energy and Mass Balance Model

We established the distributed coupled energy balance–snow/firn model (EBFM) and subsurface model for Sangqu Glacier. This model describes the evolution of vertical temperature, density, and water content profiles within the snow/ice pack, incorporating percolation and refreezing processes (Van Pelt et al., 2012). The EBFM has been successfully applied to mountain glaciers, including Abramov Glacier in the Pamir Alay (Kronenberg et al., 2022) and Kuoqionggangri Glacier in the Nyainqêntanglha Mountains (Zhu et al., 2024b). Detailed model descriptions are provided by Van Pelt et al. (2012, 2019). The sum of each surface energy component is equal to the melt energy (Q_M) and the surface energy balance formula is as follows (Van Pelt et al., 2012):

$$Q_M = S_{net} + l_{net} + Q_H + Q_L + Q_G \quad (1)$$

S_{net} is the net shortwave radiation, which consists of the incoming (S_{in}) and outgoing (S_{out}) shortwave radiation. The S_{out} depends on the albedo of the glacier surface. L_{net} is the difference between the incoming (L_{in}) and the outgoing longwave radiation (L_{out}). Q_H and Q_L are the sensible and latent heat fluxes, respectively. Q_G represents the snow and ice heat flux. The subsurface heat flux Q_G in EBFM is computed by solving the one-dimensional heat conduction equation. Following established approaches for polythermal glaciers (van Pelt et al., 2012), the effective thermal conductivity is parameterized as a function of snow/firn/ice density based on Ostin and Andersson (1991) and Sturm et al. (1997). The heat capacity is treated as a function of temperature following Yen (1981). Following micrometeorological convention, energy fluxes directed towards the surface are positive. The dichotomous iterative method was used to calculate the glacier's surface temperature, and the surface temperature was constrained at less than 0°C.

~~where S_{net} is the net shortwave radiation, which consists of the incoming (S_{in}) and outgoing (S_{out}) shortwave radiation. The S_{out} depends on the albedo of the glacier surface. L_{net} is the difference between the incoming (L_{in}) and the outgoing longwave radiation (L_{out}), where Q_H and Q_L are the sensible and latent heat fluxes, respectively. Q_G represents the snow and ice heat flux. Following micrometeorological convention, energy fluxes directed towards the surface are positive. The dichotomous iterative method was used to calculate the glacier surface temperature, and the surface temperature was constrained at less than 0°C.~~

The glacier mass balance on TP comprises four primary processes: snowfall, melting, sublimation/evaporation, and refreezing at the glacial surface. The surface mass balance components at each grid point can be expressed as:

$$B = P - M - E_{eva/sub} + C_{rf} \quad (2)$$

B denotes the point mass balance of each grid. P is for precipitation. M is the amount of melt on glacier surface. $E_{eva/sub}$ refers to the sublimation and evaporation. C_r is for refreezing. Surface ablation involves melting, sublimation and evaporation. In this study, sublimation and evaporation were quantified based on latent heat flux

and surface temperature. Specifically, the phase transition criteria were defined as follows: sublimation was identified under conditions where surface temperatures remained below the melting point while latent heat flux exhibited negative values. Conversely, evaporation was classified when surface temperatures exceeded the melting point with concurrent negative latent heat flux values. Additionally, the model explicitly includes deposition and condensation processes, which are strictly governed by positive latent heat flux conditions. Here, deposition occurs when surface temperatures remain below the melting point with positive latent heat flux, while condensation occurs when surface temperatures exceed the melting point with positive latent heat flux. However, both processes were excluded from the final analysis due to their negligible impact on the overall mass balance. Mass accumulation comprises snowfall and refreezing processes. Specifically, surface accumulation was derived from solid precipitation events, determined by a temperature-dependent rain-snow transition threshold applied to atmospheric forcing data. Subsurface liquid water sources, including meltwater, rainfall, and condensation, were tracked as potential contributors to refreezing.

~~where B denotes the point mass balance of each grid. P is for precipitation. M is the amount of melt on glacier surface. $E_{eva/sub}$ refers to the sublimation and evaporation. C_{rf} is for refreezing. Surface ablation involves melting, sublimation and evaporation. In this study, sublimation and evaporation were quantified based on latent heat flux and surface temperature. Specifically, the phase transition criteria were defined as follows: sublimation was identified under conditions where surface temperatures remained below the melting point while latent heat flux exhibited negative values. Conversely, evaporation was classified when surface temperatures exceeded the melting point with concurrent negative latent heat flux values. Additionally, the model explicitly includes deposition and condensation processes, which are strictly governed by positive latent heat flux conditions. Here, deposition occurs when surface temperatures remain below the melting point with positive latent heat flux, while condensation occurs when surface temperatures exceed the melting~~

~~point with positive latent heat flux. However, both processes were excluded from the final analysis due to their negligible impact on the overall mass balance. Mass accumulation comprises snowfall and refreezing processes. Specifically, surface accumulation was derived from solid precipitation events, determined by a temperature-dependent rain-snow transition threshold applied to atmospheric forcing data. Subsurface liquid water sources including meltwater, rainfall, and condensation were tracked as potential contributors to refreezing events.~~

In this study, the EBFM was driven by air temperature, relative humidity, wind speed, total precipitation, and cloud fraction at hourly intervals from October 2019 to September 2022. To obtain the air temperature, relative humidity, wind speed, total precipitation, and cloud fraction at hourly intervals from October 2019 to October 2021 and August 2022 to September 2022, meteorological data were reconstructed at hourly intervals using the random forest method by combining the air temperature, relative humidity, wind speed, and incoming shortwave radiation measured at AWS and ERA5. Cross-validation techniques were also employed for the correction of ERA5 data. Specifically, a 3-fold cross-validation approach was implemented for modeling relative humidity and wind speed. In contrast, for air temperature and S_{in}, our tests indicated that a 10-fold cross-validation method was more suitable. The correlation coefficients (R) were used to evaluate the simulation results. The R for air temperature, relative humidity, wind speed, and incoming shortwave radiation were 0.99, 0.88, 0.92, and 0.87 for the measurements and simulations on a daily scale (Figure. A1). The cloud fraction was defined as the ratio of incoming shortwave radiation to total radiation at the top of the atmosphere. The hourly calculation of S_{TOA} (total radiation from the top of the atmosphere) was based on elevation, slope, and aspect parameters (Hock & Holmgren, 2005). The glacier-wide mass balance was calculated using the cloudiness calculation method of Favier et al. (2004). Comparison with the (S_{in}/S_{TOA}) calculation gives a root mean square error (RMSE) of 139.89 mm w.e., a coefficient of determination (R^2) of 0.71 and a percentage bias (PBIAS) of 18.4%. We also estimated the total precipitation on Sangqu Glacier from

October 2019 to September 2022. This was achieved by combining total precipitation data from ERA5 with data from direct measurements. First, we calculated the ratio (0.54) of total measured precipitation to that estimated by ERA5 for the overlap period (October 2020 to July 2022). Then, the ratio was used to correct all reanalysis precipitation data from October 2019 to September 2021. This approach has been extensively utilized in glacier–related studies on TP (Yang et al., 2013; Potocki et al., 2022; Zhu et al., 2024a).

In this study, the EBFM was applied as a distributed model at a spatial resolution of 100 m and hourly temporal resolution, driven by air temperature, relative humidity, wind speed, total precipitation, and cloud fraction from October 2019 to September 2022. To obtain the air temperature, relative humidity, wind speed, total precipitation, and cloud fraction at hourly intervals from October 2019 to October 2022, meteorological data were reconstructed at hourly intervals using the Random Forest method by combining the air temperature, relative humidity, wind speed, and S_{in} measured at AWS and ERA5. This study applies the Random Forest method for statistical downscaling of ERA5 reanalysis data to reconstruct near-surface meteorological variables, specifically air temperature, relative humidity, wind speed, and S_{in} at a glacier surface AWS site.

Observational data from an AWS were first spatially and temporally matched with ERA5 grid points to construct training and testing datasets. Predictor variables included surface variables (2 m air temperature, dewpoint temperature, 10 m wind components, and surface pressure) and at 300 hPa and 500 hPa (temperature, humidity, wind components, and geopotential height), from which derived variables such as wind speed and relative humidity were also computed. To minimize overfitting and obtain robust estimates of model performance, we applied three repetitions of five-fold cross-validation, where the training data were repeatedly split into five subsets, each serving in turn as the validation set. Evaluation results indicate that the Random Forest model achieves high predictive accuracy. Comparisons between the downscaled estimates and in-situ observations yielded R^2 (coefficient of

411 determination) values of 0.99, 0.96, 0.94, and 0.96 for air temperature, relative
412 humidity, wind speed, and S_{in}, respectively, at the hourly scale (Fig. S1), with
413 similarly robust performance during the ablation season (June–September) (Fig. S8).
414 The cloud fraction was defined as the ratio of incoming shortwave radiation to
415 total radiation at the top of the atmosphere. The hourly calculation of S_{TOA} (total
416 radiation from the top of the atmosphere) was based on elevation, slope, and aspect
417 parameters (Hock & Holmgren, 2005). We also estimated the total precipitation on
418 Sangqu Glacier from October 2019 to September 2022. This was achieved by
419 combining total precipitation data from ERA5 with data from direct measurements.
420 First, we calculated the ratio of total measured precipitation to that estimated by
421 ERA5 for the overlap period (October 2020 to July 2022). Then, the ratio was used to
422 correct all reanalysis precipitation data from October 2019 to September 2021. This
423 approach has been extensively utilized in glacier–related studies on TP (Zhu et al.,
424 2024b).
425 The spatial interpolation of meteorological data considered the topographic
426 conditions (elevation, slope, and aspect) of Sangqu Glacier. The mean air temperature
427 lapse rate was 0.6°C/1000 m. Precipitation gradient was the parameter for the EBFM
428 model, considering glacier mass balance and albedo. Following the approach of Hock
429 and Holmgren (2005) in their distributed surface energy-balance modeling for
430 Storglaciären, Sweden, the wind speed and relative humidity measured at the single
431 AWS are assumed to be representative of the entire glacier, due to the limited
432 availability of spatially distributed observations and the relatively small spatial
433 variability in relative humidity across the glacier.
434 The methodology for calculating the energy balance components at the glacier
435 surface was based on the findings of previous studies. The S_{in} was described as
436 described by Klok and Oerlemans (2002) and Van Pelt et al. (2012) and accounts for
437 the grid aspect and shading by the surrounding terrain. S_{out} depends on surface albedo.
438 Snow albedo was related to temperature and humidity (Oerlemans and Knap, 1998;
439 Bougamont et al., 2005; Van Pelt et al., 2019), and ice albedo was calculated using the

dew point temperature (Mölg et al. (2008). The L_{in} was calculated based on the relative humidity and air temperature (Brunt, 1932). L_{out} was calculated using the Stefan–Boltzmann law. Q_H and Q_L were calculated using the method proposed by Klok and Oerlemans (2002). Q_G was obtained as the sum of the conductive heat fluxes (Reijmer and Hock, 2008; Van Pelt et al., 2012).

~~The spatial interpolation of meteorological data considered the topographic conditions (elevation, slope, and aspect) of Sangqu Glacier. The mean air temperature lapse rate was 0.65°C/100 m. Precipitation gradient was the parameter for the EBFM model, taking into account glacier mass balance and albedo. The wind speed and relative humidity measured at the AWS represented the entire glacier. The methodology for calculating the energy balance components at the glacier surface was based on the findings of previous studies. The S_{in} was simulated as described by Klok & Oerlemans (2002) and Van Pelt et al. (2012) and accounts for the grid aspect and shading by the surrounding terrain. S_{out} depends on surface albedo. Snow albedo was related to temperature and humidity (Oerlemans and Knap, 1998; Bougamont et al., 2005; Van Pelt et al., 2019), and ice albedo was calculated using the dew point temperature (Mölg et al. (2008). The L_{in} was calculated based on the relative humidity and air temperature (Brunt, 1932). L_{out} was calculated using the Stefan–Boltzmann law. Q_H and Q_L were calculated using the method proposed by Klok & Oerlemans (2002). Q_G was obtained as the sum of the conductive heat fluxes (Reijmer & Hock, 2008; Van Pelt et al., 2012).~~

~~The interpolation of meteorological data at the glacier scale, as well as the area-averaged energy and mass balance, are related to the surface elevation of glaciers. Beckmann et al. (2023) found the surface elevation feedback largely amplifies melting for scenarios with and without extremes, with additional mass loss attributed to this feedback having the greatest impact on projected sea level. In this study, we employ sensitivity analysis to examine the extent to which the mass balance of the Sangqu Glacier responds to variations in surface elevation. With SRTM data serving as the benchmark for surface elevation, we established ten experimental scenarios~~

encompassing changes of +2 m, +5 m, +10 m, +20 m, and +50 m (alongside corresponding decreases of −2 m, −5 m, −10 m, −20m, and −50 m). Throughout these experiments, parameters related to air temperature, total precipitation, and albedo were held constant while the model was executed. The sensitivity analysis reveals that, when considering the scenarios with positive changes (+2m to +50m), the magnitude of the mass balance response to surface elevation variations on Sangqu Glacier amounts to 9.4 mm w.e. m^{-1}. In contrast, for the scenarios with negative changes (−2 m to −50 m), the magnitude of the response increases to 12.6 mm w.e. m^{-1}. The terrain-associated feedback mechanism has the potential to exacerbate glacier mass loss on TP when faced with decreasing glacier surface elevation.

The standardized heatwave index (S_{HI}) was employed to detect heatwave events (Raei et al., 2018; Shan et al., 2024). This index quantifies temperature deviations relative to 30-year climatological norms. It ranks heatwaves by their recurrence probability within a dynamic reference period. The reference period and climate normal for calculating such probabilities must be carefully chosen because of the non-stationarity of temperature records caused by global warming. Following Shan et al. (2024), we implemented a 30-year moving window to address non-stationarity. Therefore, we used the past 30 years as the historical reference period and averaged the daily values. The S_{HI} was calculated for each day as follows (Raei et al., 2018; Shan et al., 2024):

$$\overset{\Lambda}{T}_{m,j} = \begin{cases} \dfrac{1}{N_h} \sum_{j=i-N_h+1}^{i} T_{m,j} & if \geqslant N_h \\ \dfrac{1}{N_h}\left(\sum_{j=365-N_h+i+1}^{365} T_m - 1, j + \sum_{j=1}^{i} T_{m,j} \right) & if < N_h \end{cases} \quad (3)$$

$$S_{HI}^{m,j} = \Phi^{-1}\left(F_{m,j}^{h}\left(\overset{\Lambda}{T}_{m,j} \right) \right) \quad (4)$$

where i and j represent calendar days. M is the number of years of historical observations, and $\overline{T}_{m,j}$ (℃) is the daily mean temperature at day i of year M. N_h is the length of the accumulation period for a heatwave; $\overset{\Lambda}{T}_{m,j}$ is the mean temperature over

~~the accumulation period up to and including day i. $F^{h}_{m,j}$ is the cumulative distribution function (CDF). Φ^{-1} is an inverse standard normal CDF. In this study, we calculated the average between February 28 and 29, subsequently removed the leap day (February 29) to maintain a 365-day annual cycle. We set up a 3-day averaging window to run the S_{HI} program and used S_{HI} value greater than 1 to identify heat waves.~~

4.2 Modelling Validation and Uncertainty

To reduce uncertainties arising from manual parameter calibration, this study proposes a stepwise parameter calibration scheme. First, the SCE-UA algorithm (Duan et al., 1992) was employed to calibrate parameters related to incoming longwave radiation parameterization using RMSE as the objective function. Subsequently, for the EBFM model, the NSGA-II multi-objective optimization algorithm (Deb et al., 2002) was applied. Utilizing daily-scale surface albedo data from on-glacier meteorological stations and glacier-wide mass balance observations, the EBFM parameters were calibrated with both the R^2 and RMSE as dual objective functions.

Following parameter calibration, the model's performance was rigorously validated using in-situ observational data to the greatest extent possible. Specifically, validation utilized in situ measurements of albedo, L_{in}, and L_{out} from an AWS installed on the glacier. Additionally, point-scale mass balance data across different elevations, along with glacier-wide mass balance records for the periods October 2019–October 2020, October 2020–October 2021, and October 2021–July 2022, were used to assess the simulation accuracy. To further evaluate the model's performance in simulating glacier mass balance, seasonal-scale glacier-wide mass balance data observed during 2020–2021 were also employed.

Fig 2 presents a comparison between measured and modelled albedo, L_{in}, and L_{out} at the AWS site. Daily albedo simulations showed good agreement with observations, with an R of 0.76 and an RMSE of 0.1 (Fig. 2a). This agreement improved for 7-day average values (R = 0.74, RMSE = 0.09; Fig. S2). Simulations of L_{in} and L_{out} were

also robust. Modelled L_{in} correlated well with measurements (R = 0.9, RMSE = 22 W m^{-2}; Fig. 2b), as did L_{out} (R = 0.95, RMSE = 11 W m^{-2}; Fig. 2c). The high accuracy in simulating radiation components supports reliable estimates of L_{net} and glacier surface temperature.

The performance of the EBFM model in simulating glacier mass balance was evaluated using multi-scale comparisons. At the point scale, the RMSE between simulated and observed mass balances was 288 mm w.e. (Fig. 2e), while at the glacier-wide scale, the RMSE decreased to 101 mm w.e. (Figs. 3f and 3g). Moreover, the simulated cumulative mass balance from 1 October 2019 to 30 September 2022 closely matched observations (Fig. 3g). We also compared the differences between observed and simulated temperatures at 3 m and 5 m within the glacier, with correlation coefficients of 0.94 and 0.96, respectively (Fig. S3).

To assess model accuracy at seasonal resolution, we compared simulated and in situ mass balances for the 2020–2021 balance year, yielding an RMSE of 329 mm w.e. (Fig. 2d). We also compared our simulated 2021–2022 mass balance for Sangqu Glacier with independent estimates. The simulated value (−919 mm w.e.) closely agreed with in-situ observations from the neighbouring Xiao Dongkemadi Glacier (−881 mm w.e.; Zhu et al., 2026a), further confirming model consistency. In contrast, the satellite-derived product of Dussaillant et al. (2025) reported −1278 mm w.e. for Sangqu Glacier, which is more negative than our result (Fig. 2h). Despite this numerical difference, all independent lines of evidence, including our model, the in-situ data from Xiao Dongkemadi Glacier (Zhu et al., 2026a), and the global assessment of Dussaillant et al. (2025), suggest that 2021–2022 was likely an extreme mass loss year for Sangqu Glacier.

Collectively, these multi-scale and cross-site comparisons demonstrate that the EBFM model provides reliable energy and mass balance simulations for Sangqu Glacier, thereby supporting its use for detailed analyses of energy and mass balance processes.

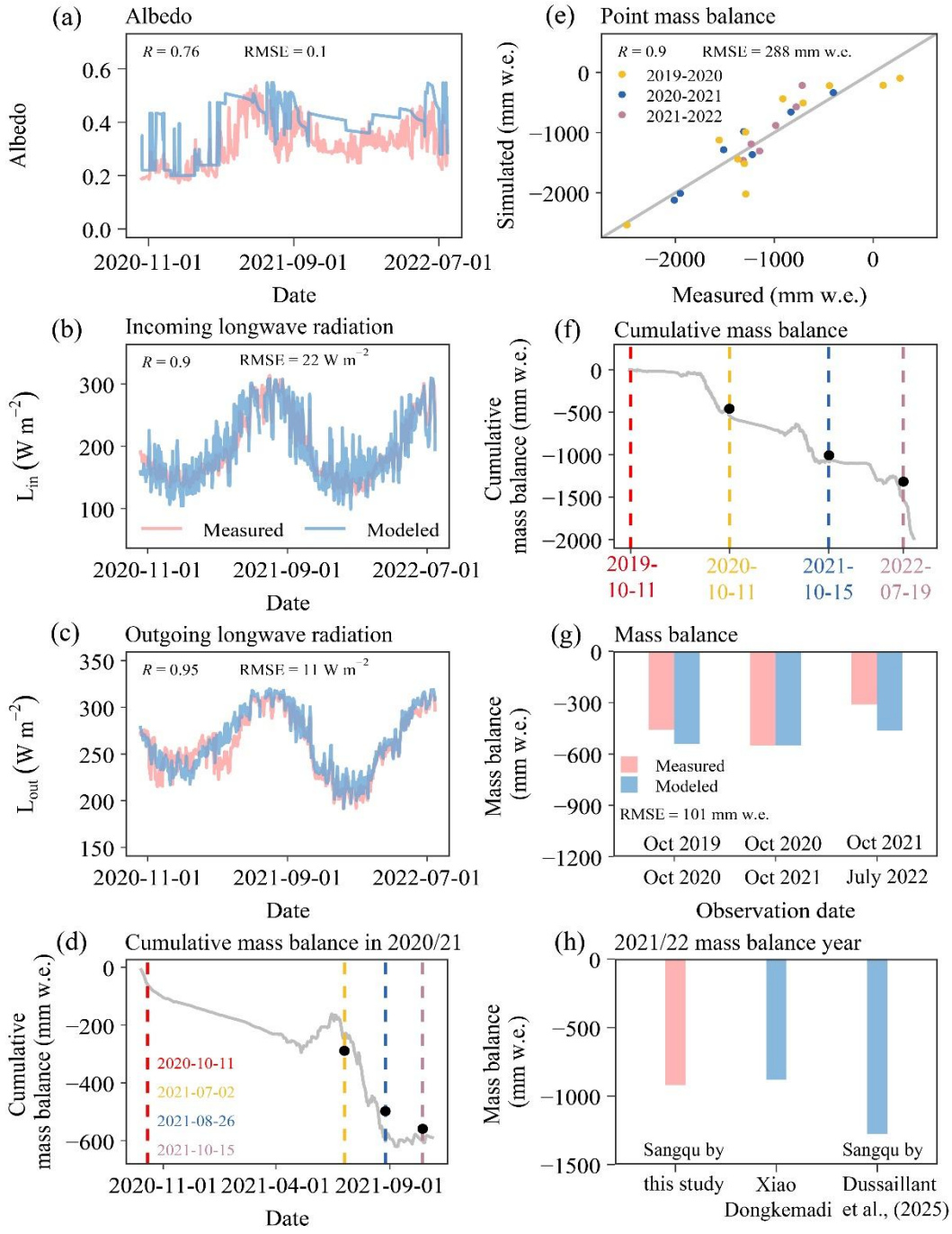


Figure 2. Comparison between observations and simulations of (a) albedo, (b) L_{in}, (c) L_{out}, (d) glacier mass balance from June to September 2021, (e) point mass balance at different elevations, (f) accumulation mass balance, and (g) glacier-wide mass balance for the periods 2019/20, 2020/21, and from October 2021 to July 2022. (h) Comparison of simulated glacier mass balance for Sangqu Glacier in 2021/22 with observed mass balance for Xiao Dongkemadi Glacier.

This study conducts sensitivity and uncertainty tests based on the parameter

selection framework proposed by Van Pelt et al. (2012). Model output uncertainty primarily originates from key parameters governing albedo (snow, firn, and ice), precipitation gradients, critical temperature thresholds (e.g., the rain-snow partitioning threshold), temperature lapse rate, parameters for downward shortwave radiation, and turbulent flux calculations, all of which are crucial determinants of mass balance simulation accuracy. Following the recommendation of Van Pelt et al. (2012), an uncertainty of ±0.03 was applied to the albedo of snow, ice, and firn, along with the relevant parameters. The aerosol transmissivity coefficient, a parameter influencing S_{in}, was perturbed by ±0.01. The temperature lapse rate was adjusted by ±0.1 °C /1000 m. All other parameters were perturbed by ±10% to assess sensitivity and associated uncertainty. The sensitivity was quantified using the formula provided below (Oerlemans et al., 1998):

$$\frac{dM}{dS} = \frac{M(S_H) - M(S_L)}{2} \quad (3)$$

M is the glacier-wide mass balance, and S represents the parameter for which sensitivity tests are to be performed.

The results of the sensitivity tests are presented in the supplementary materials (Tables S1-S6). The glacier-wide mass balance of the Sangqu Glacier exhibits particularly high sensitivity to ice and snow albedo. Specifically, the sensitivities to parameters related to snow, firn, and ice albedo are 123.2, 114.7, −0.3, and 126.3 mm w.e. a^{-1}, respectively. The temperature lapse rate shows a sensitivity of -141.4 mm w.e. a^{-1}. The background turbulent exchange coefficient and turbulent flux coefficient yield sensitivities of 8.3 and -55 mm w.e. a^{-1}, respectively. In comparison, the sensitivity of the glacier-wide mass balance to the rain-snow temperature threshold and precipitation gradient are relatively minor, at 0.5 and −2.2 mm w.e. a^{-1}, respectively. The sensitivity to the aerosol transmissivity coefficient is −20.2 mm w.e. a^{-1}. The glacier-wide annual mass balance has a sensitivity of −9.9 mm w.e. a^{-1} to effective thermal conductivity and +10.5 mm w.e. a^{-1} to heat capacity.

The total uncertainty in the modelled mass balance for each mass balance year

was estimated following the error propagation law described by Zhu et al. (2024a) and Zhu et al. (2021). The average uncertainty over three mass balance years is 264.3 mm w.e. (Tables S2-S4). A comprehensive sensitivity analysis of key model parameters during the heatwave period was conducted, and the associated uncertainty in melt amount was estimated to be 99.3 mm w.e. (Table S1).

~~Model validation utilized in situ measurements of albedo, S_{in}, L_{in}, and L_{out} from AWS to evaluate EBFM performance. The point mass balance at different elevations on the glacier surface and glacier-wide mass balance measured during October 2019–October 2020, October 2020–October 2021, and October 2021–July 2022 was used to assess the accuracy of the EBFM model simulations.~~

~~Figure. 2 shows the results of comparing the measured and modelled albedo, S_{in}, L_{in}, and L_{out} at the AWS sites. The measured and modelled albedo show good agreement, with RMSE and R of 0.1 and 0.68 at daily scale, respectively (Figure. 2a). The RMSE and R for weekly scale observations and modelled albedo are 0.09 and 0.76, respectively (Figure. S1). Observed and modelled albedos during extreme heat waves (30 May to 9 June and 3 July to 16 July) were also compared, with RMSE and R of 0.14 and 0.77, respectively. The measured and modelled R and RMSE of S_{in} were 0.9 and 32.4 W m^{-2}, respectively (Figure. 2b). Discrepancies between observed and simulated S_{in} were mainly due to errors in the estimated cloud fraction (Van Pelt et al., 2012). Good agreement between the measured and modelled albedo and S_{in} ensures the accuracy of S_{net}, which is the main energy source at the glacier surface. The L_{in} R and RMSE of the measured and modelled are 0.88 and 26.2 W m^{-2}, respectively (Figure. 2c). The L_{out} R and RMSE of the measured and modelled are 0.95 and 10.6 W m^{-2}, respectively (Figure. 2d). This good agreement ensures the accuracy of the net longwave and surface temperature simulations of the surface energy balance.~~

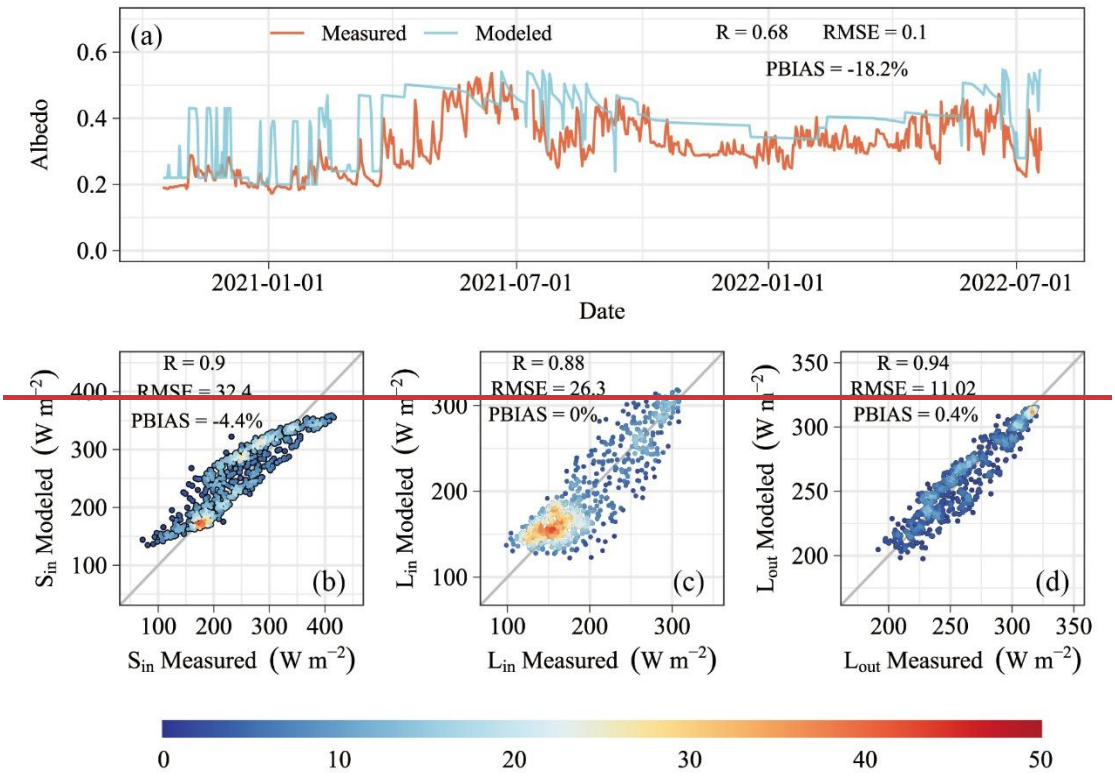


Figure 2. Comparison of (a) albedo in daily scale, (b) S_{in}, (c) L_{in}, and (d) L_{out}, measured and modelled at the AWS sites on Sangqu Glacier.

We also compared the measured and modelled mass balances. The RMSE of the measured and modelled point mass balances was 297 mm w.e. (Figure. 3a). The RMSE of the measured and modelled glacier wide mass balance was 211 mm w.e. (Figure. 3b). We also present comparisons between observations and model simulations for the periods October 2019–October 2020, October 2020–October 2021, and October 2021–July 2022 (Figure. 3c, d, and e). RMSE values between simulated and observed results were 322, 256, and 293 mm w.e., respectively. This consistency allowed us to analyze the seasonal and interannual characteristics of the surface energy and mass balance of Sangqu Glacier.

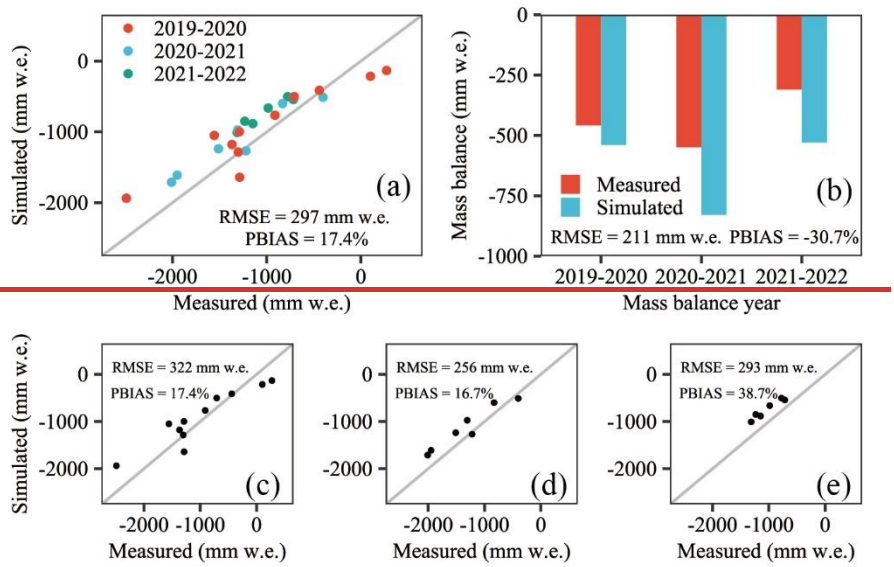


Figure. 3. Comparison of measured and modelled mass balance at (a) point scale and (b) glacier-wide scale. (c), (d) and (e) are point scale comparisons of the mass balance measurements and modelling for the years 2019-2020, 2020-2021 and 2021-2022 respectively. 2019–2020 refers to October 2019 to October 2020 and also 2020–2021. 2021–2022 refers to October 2021 through July 2022.

The uncertainty in model outputs arises primarily from key parameters governing albedo (snow, firn, and ice), precipitation gradients, critical temperature thresholds, and turbulent flux calculations, all of which critically determine mass balance simulation accuracy. Following standard sensitivity analysis protocols in glaciology, we implement a ±10% parameter perturbation approach, a methodology ubiquitously adopted in both degree-day and energy mass balance modeling frameworks for systematic uncertainty quantification. Snow albedo and firn albedo (±0.03) uncertainties were used as recommended by Van Pelt et al. (2012). The total uncertainty for the modelled mass balance in each year was estimated using the error propagation law described by Zhu et al. (2024b) and Zhu et al. (2021). The uncertainty in the mass balance averaged over three years was 222.9 mm w.e. (Table S2, S3, and S4). The uncertainty of the melt during extreme heat waves has also been discussed and was found to be 150.2 mm w.e. (Table S1).

4.3 A Dual-Threshold Framework for Identifying Extreme Mass Loss Events in Short-Term Glacier Mass Balance Records

Accurately identifying extreme mass balance events across different temporal

scales is crucial for advancing our understanding of the characteristics and mechanisms underlying glacier mass balance responses to climate change. Although conventional approaches such as percentile thresholds (Vargo et al., 2020) (e.g., 10th percentile) and generalized extreme value (GEV) distributions (Thibert et al., 2018) have been widely employed to detect extreme mass loss and melt events, these methods require long-term mass balance records exceeding 30 years. On TP, only Xiao dongkemadi Glacier possesses a continuous observational mass balance series longer than three decades, with monitoring initiated in 1989 (Yao et al., 2012). Most other reported glacier mass balance records in this region typically span less than 10 years. To address this limitation, we compiled available observed and reconstructed annual mass balance data across TP and developed a novel methodology capable of reliably identifying extreme mass loss events from short-term records (under 10 years).

This study proposes a dual-threshold extreme event detection method based on quantile-statistical distribution coupling. The mathematical framework is constructed as follows: First, the glacier mass balance (m_b) time series is partitioned into training and test sets, where the training data is denoted as $\{m_{b,i}\}_{i=1}^{n}$ with corresponding years $\{y_i\}_{i=1}^{n}$. The baseline criterion for extreme events is defined using the p-quantile threshold of the training set:

$$Q_p = Inf\{m_b \in R | F_n(m_b) \geq p\} \quad (5)$$

Where Q_p denotes the p-quantile threshold for extreme event identification. $F_n(m_b)$ corresponds to the empirical cumulative distribution function of the training set mass balance data. $p \in (0,1)$ defines the target probability level (default $p = 0.1$) for extreme event selection.

To establish the statistical distribution criterion, we calculate the training set parameters:

$$\mu = \frac{1}{n}\sum_{i=1}^{n} m_{b,i} \tag{6}$$

$$\sigma = \sqrt{\frac{1}{n-1}\sum_{i=1}^{n}\left(m_{b,i} - \mu\right)^2} \tag{7}$$

Where μ represents the mean of training set mass balance values. σ quantifies the standard deviation of training set mass balance values. n indicates the total number of training years. $m_{b,i}$ refers to the mass balance measurement in the i training year.

A parameter space traversal algorithm is employed to solve for the statistical threshold parameter kk that satisfies the equivalence conditions:

$$\begin{cases} \mu - K\sigma \leqslant Q_p \\ \{y_i | m_{b,i} < \mu - K\sigma\} \equiv \gamma_T \end{cases} \tag{8}$$

Where K controls the multiplier of standard deviations from the mean. $\mu - K\sigma$ specifies a candidate statistical threshold constrained by the quantile boundary Q_p. γ_T comprises years identified as extreme events through the quantile criterion.

Let the solution set be $K \in [K_{\min}, K_{\max}]$, we then construct dual detection thresholds:

$$\begin{aligned} T_{strict} &= \mu - K_{\max}\sigma \ \ (strict\ threshold) \\ T_{relaxed} &= \mu - K_{\min}\sigma \ \ (relaxed\ threshold) \end{aligned} \tag{9}$$

where $K_{\max}$ and $K_{\min}$ define the maximum and minimum valid scaling coefficients satisfying the equivalence conditions, while T_{strict} and $T_{relaxed}$ delimit the strict and relaxed thresholds that respectively ensure full consistency with historical extremes and complete coverage of quantile-defined events. During testing, a year y_i is classified as an extreme event if $m_{b,i} < T_{relaxed}$, while $m_{b,i} < T_{strict}$ indicates a high-confidence extreme event.

This method achieves mathematical equivalence between quantile-based and

~~statistical distribution criteria through feasible region solving of parameter K. The dual-threshold design effectively quantifies uncertainty boundaries in detection results, maintaining consistency with historical extreme event definitions while enhancing model adaptability to distribution characteristics.~~

4.3 Standardized heatwave index

The standardized heatwave index (S_{HI}) was employed to detect heatwave events (Raei et al., 2018; Shan et al., 2024). This index quantifies temperature deviations, ranking heatwaves by their probability of occurrence relative to a climatological reference period. As highlighted by Shan et al. (2024), the choice of this reference period is critical due to the non-stationarity of temperature records caused by global warming. Using the entire period of record can introduce bias, as the climate normal for a given day would be influenced by long-term trends rather than representing the recent expected conditions to which ecosystems and society may have adapted.

To address this, Shan et al. (2024) explicitly recommend using a dynamic, 30-year moving window to better account for climate non-stationarity. Following their methodology, we used the past 30 years as the historical reference period (1992-2021). For each target day, the 30-year mean of the accumulated temperature is calculated and used as the expected normal, allowing the index to reflect anomalies relative to a recent, locally adapting baseline. The S_{HI} for each day was then calculated as follows (Raei et al., 2018; Shan et al., 2024):

$$\hat{T}_{m,i}=\begin{cases}\dfrac{1}{N_{\mathrm{h}}}\displaystyle\sum_{j=i-N_{\mathrm{h}}+1}^{i}T_{m,j}, & \text{if } i\geq N_{\mathrm{h}}\\[2ex] \dfrac{1}{N_{\mathrm{h}}}\left(\displaystyle\sum_{j=365-N_{\mathrm{h}}+i+1}^{365}T_{m-1,j}+\sum_{j=1}^{i}T_{m,j}\right), & \text{if } i<N_{\mathrm{h}};\end{cases} \tag{4}$$

$$\mathrm{S}_{\mathrm{HI}m,i}=\Phi^{-1}\left(F_{m,i}^{\mathrm{h}}\left(\hat{T}_{m,i}\right)\right) \tag{5}$$

The variables i and j denote calendar days, with $i,j\in\{1,2,\cdots,365\}$; $m\in\{1,2,\cdots,M\}$ represents the year, M is the total number of years in the historical

record. The daily mean temperature $T_{m,i}$ for day i of year m is used directly. For leap years, the mean temperatures of February 28 and February 29 are averaged and assigned to February 28, after which the leap day is excluded. The accumulation period for a heatwave is denoted by N_h, and $\hat{T}_{m,i}$ represents the mean temperature over the accumulation period ending on day i. The cumulative distribution function (CDF) $F^h_{m,i}$ is fitted to the set $\{\hat{T}_{m,i}, \hat{T}_{m-1,i}, \cdots, \hat{T}_{m-29,i}\}$ when $m \geq 30$; otherwise, it is fitted to $\{\hat{T}_{30,i}, \hat{T}_{29,i}, \cdots, \hat{T}_{1,i}\}$. The inverse of the standard normal CDF is denoted as Φ^{-1}, and $S_{HIm,i}$ is the resulting standardized heatwave index for day i of year m.

Fig 3 presents the identified heatwave events (Figs. 3a, 3c and 3e) and the associated air temperature anomaly magnitudes (Figs. 3b, 3d and 3f). The anomalies are calculated relative to the 1992–2021 climatology. The first dataset consists of in-situ observations from the Tuotuohe meteorological station, located approximately 150 km from Sangqu Glacier. This station has been widely employed in previous studies on glacier mass balance and hydrological processes in the region (Gao et al., 2012). Using daily mean air temperatures from this station, three heatwave events were identified: 1–9 June, 3–16 July, and 3–29 August (Figs. 3a and 3b). The second dataset is derived from the ERA5 reanalysis, specifically from the grid cell corresponding to the Tuotuohe meteorological station. Based on daily mean air temperatures extracted from this dataset, three heatwaves were identified: 1–8 June, 7–15 July, and 4 August–1 September (Figs. 3c and 3d). The third dataset is also from ERA5 reanalysis but represents the grid cell covering the study site, Sangqu Glacier. Analysis of daily mean air temperatures from this dataset revealed three heatwave periods: 1–10 June, 7–17 July, and 2 August–1 September (Figs. 3e and 3f).

To minimize uncertainties arising from the use of multiple data sources, only the overlapping periods consistently identified by all three datasets were defined as the final heatwave events (Fig. 3g). Accordingly, the three heatwave events in the summer of 2022 were delineated as 1–8 June, 7–15 July, and 4–29 August. Fig 3h shows that

the air temperature anomaly magnitudes on the Sangqu Glacier AWS during the summer heatwaves of 2022 were 4.9 °C, 1.6 °C, and 2 °C, respectively.

This approach, which integrates multi-source data consistency with a rigorous objective statistical method for defining event extremity and independence, effectively resolves discrepancies among different datasets and enhances the reliability of the heatwave identification.

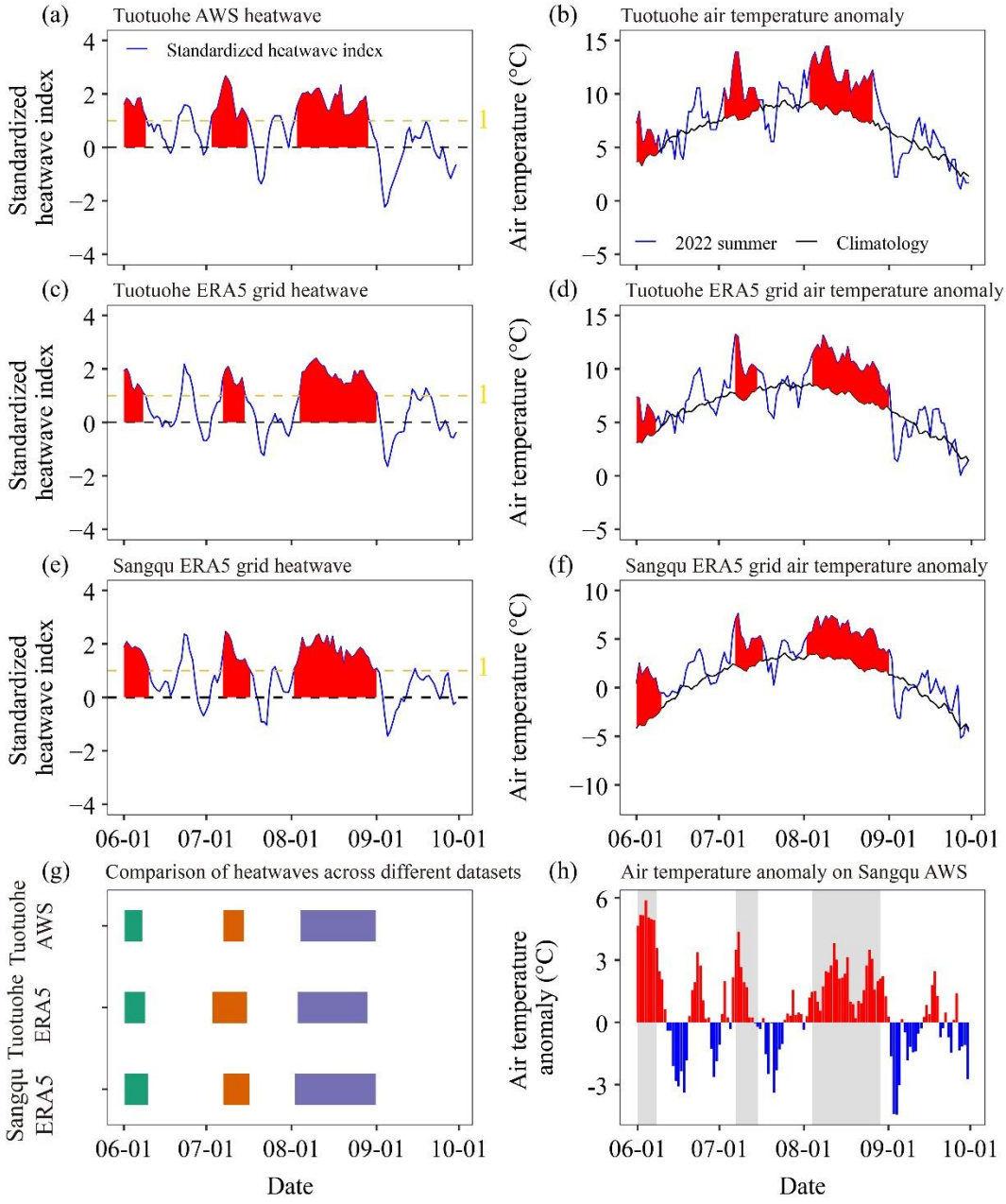


Figure 3. Identification of heatwave events from June to September 2022. Air temperature anomalies are calculated relative to the 1992–2021 climatology. (a, b) Heatwave events and

corresponding temperature anomalies at the Tuotuohe meteorological station. (c, d) As in (a, b), but for the ERA5 grid cell containing the Tuotuohe meteorological station. (e, f) As in (a, b), but for the ERA5 grid cell containing Sangqu Glacier. In panels (a), (c), and (e), the yellow line marks the standardized heatwave index threshold of 1; a heatwave is identified when the index exceeds this threshold for at least three consecutive days. (g) Comparison of heatwave events identified from the three datasets shown in (a), (c), and (e). (h) Summer (June–September) temperature anomalies at Sangqu Glacier in 2022 based on the identified heatwave events.

4.4 A Dual-Threshold Framework for Identifying Extreme Mass Loss Events in Short-Term Glacier Mass Balance Records

Conventional approaches for detecting extreme mass loss events, such as percentile thresholds (Vargo et al., 2020) and generalized extreme value (GEV) distributions (Thibert et al., 2018), typically require observational records exceeding 30 years. On the Tibetan Plateau, however, most glacier mass balance series span less than a decade, with the sole exception of Xiao Dongkemadi Glacier (since 1989; Yao et al., 2012). To address this limitation, we developed a dual-threshold framework capable of reliably identifying extreme mass loss events from short-term records (<10 years).

The core idea is to establish a mathematical link between two approaches for defining extreme events within a training period: a percentile-based method and a method based on deviations from the mean. Let B_y denote the annual mass balance (mm w.e.). The available record is split into a training set (years T_{train}) and a test set (years T_{test}). The training set is used to calibrate the relationship between the two methods, and the calibrated rule is then applied to the test set.

First, we identify extreme years in the training set using a percentile-based threshold. With a default probability level $p = 0.10$ (the 10th percentile), the threshold Q_P is computed, and all years in the training set with annual mass balance below Q_P are defined as extreme mass loss events, denoted by the set Y_{target}.

Second, we calculate the mean μ and standard deviation σ of the annual mass

balance in the training set:

$$\mu = \frac{1}{n}\sum_{i=1}^{n} B_i, \sigma = \sqrt{\frac{1}{n-1}\sum_{i=1}^{n}(B_i - \mu)^2} \quad (6)$$

n is the number of years in the training set, and B_i is the mass balance of the i-th training year.

Third, we determine a multiplier k such that the rule $B < \mu - k \cdot \sigma$ identifies the same extreme years as the percentile method. By searching over a predefined range (e.g., $k \in [0.5, 2.0]$), we retain all k values for which the set of years satisfying $B < \mu - k \cdot \sigma$ exactly matches Y_{target}. The smallest and largest k in this valid range are denoted k_{min} and k_{max}, respectively. These yield two thresholds:

$$\text{relaxed threshold} = \mu - k_{\min} \cdot \sigma, \ \text{strict threshold} = \mu - k_{\max} \cdot \sigma \quad (7)$$

The relaxed threshold serves as a lower bound for identifying potential extreme events, while the strict threshold denotes a more conservative bound for high-confidence extreme events. The interval between the two thresholds quantifies the uncertainty arising from the short training series.

Finally, for any year in the test set, we classify it as an extreme event if its mass balance falls below the relaxed threshold, and as a high-confidence extreme event if it falls below the strict threshold. To test the reliability and transferability of this dual-threshold framework, we validated it using five glaciers with long-term observational records across the TP, as presented in Sect. 5.2.

5. Results

5.1 Seasonal Cycle and Interannual Variation of Energy and Mass Balance

~~Seasonally varying glacier wide energy balances and their components are shown in Figure. 4a. The S_{net} shows significant seasonal variability in the range of 40 W m^{-2} to 66.3 W m^{-2}, and this variability is mainly driven by the seasonal shift in the solar elevation angle in conjunction with the glacier surface albedo. L_{net} is the major energy loss term for the glacier surface energy balance (Figure. 4a). The maximum and minimum values of net longwave radiation are −16.2 W m^{-2} and −82.3 W m^{-2},~~

which occur in August and March, respectively. The mean L_{net} in the warm and cool seasons are −31 W m^{-2} and −77.2 W m^{-2}, respectively. The difference in L_{net} between the warm and cool seasons mainly depends on the difference between L_{in} and L_{out}. In this study, L_{in} is influenced by both air temperature and relative humidity, both of which reach high values in the warm season, corresponding to higher L_{in}. The L_{out} calculated from the glacier surface temperature was also high during the warm season. Combining L_{in} and L_{out}, the absolute value of L_{net} was found to be lower during the warm season than during the cold season.

The Q_H on Sangqu Glacier were continuously above 0 W m^{-2} and was an important heat source in the energy balance (Figure. 4a). This indicates that the atmosphere continuously supplies heat to the glacier surface, which helps maintain the glacier surface temperature. The Q_H in the cold and warm seasons are 39.3 W m^{-2} and 21.5 W m^{-2}, respectively, and this difference may be closely related to the temperature gradient between the glacier surface and the atmosphere, as well as seasonal changes in wind speed. In contrast, the Q_L on Sangqu Glacier is usually less than 0 W m^{-2}, and the mean Q_L is −10.7 W m^{-2}, indicating that sublimation or evaporation processes are continuously occurring at the glacier surface (Figure. 4a).

Q_G depends on the heat transfer coefficients of ice and snow, as well as the temperature gradient (the temperature difference between the surface and the interior of the glacier). The mean Q_G is 1 W m^{-2}, indicating that the Q_G accelerates the melting process at the glacier surface (Figure. 4a). Further analysis showed that Q_G in the cold season played an important role in maintaining the energy balance of the glacier surface, whereas in the warm season, it accelerated the melting of the glacier surface. Combining the S_{net}, L_{net}, Q_H, Q_L, and Q_G, it was found that the melt energy started to be higher than 0 W m^{-2} in May, indicating that the melt on Sangqu Glacier started, with peaks in July and August (Figure. 4a).

The glacial mass balance and its components at the glacial scale are shown in Figure. 4b. Melt, snowfall, refreezing, and sublimation/evaporation are the major mass components of glaciers on the central TP. Mass replenishment comes from

~~snowfall and the refreezing of the snowpack. 73.2% of snowfall is concentrated in the warm season, and most precipitation falls as snow on glacier surfaces during the warm season. Cold season snowfall accounts for only 27% of the total snowfall, with less mass replenishment. The total snowfall in April and May, which affects warm season albedo and glacier melt rates, accounted for 13.3% of the total snowfall. Meltwater on the glacier surface and water content in the snow are the main sources of mass for refreezing. The volume of refreezing peaks in June, which is related to snow cover and meltwater on the glacier surface. During the observation period, the refreezing amount on Sangqu Glacier accounted for 4% of the melting amount.~~

~~The major mass losses from glaciers include melt, sublimation and evaporation. The melt is the dominant component of the mass balance. Melting begins at the glacier surface in May and peaks in July or August, which is related to the seasonal distribution of melt energy. 85% of melt occurs during the warm season. June, July, August, and September account for 18%, 25%, 34%, and 9% of the total melt, respectively.~~

~~Sublimation/evaporation is a component of the mass balance that cannot be ignored; in this study, sublimation/evaporation on the Sangqu Glacier accounted for 17% of the mass balance. Previous studies have shown that Sublimation and evaporation of the glacier surface, as a mass loss term, varies spatially on TP (Zhu et al., 2020; Guo et al., 2022). Sublimation and evaporation on Sangqu Glacier (=161 mm w.e. yr^{-1}) was similar to Zhadang Glacier (=154.4 mm w.e. yr^{-1}) (Zhu et al., 2018) and Qiangtang No. 1 Glacier (=175.5 mm w.e. yr^{-1}) (Li et al., 2018), lower than Guliya (=194 mm w.e. yr^{-1}) (Zhu et al., 2022b) and Muztag Ata No. 15 Glacier (=272 mm w.e. yr^{-1}) , higher than Parlung No. 4 (=144.8 mm w.e. yr^{-1}) and Parlung No. 94 Glacier (=60 mm w.e. yr^{-1}) (Yang et al., 2013; Zhu et al., 2018). Differences in sublimation and evaporation from glaciers indicate differences in the exchange of water and heat between the glacier surface and the atmosphere in different climatic zones (Zhu et al., 2020; Guo et al., 2022).~~

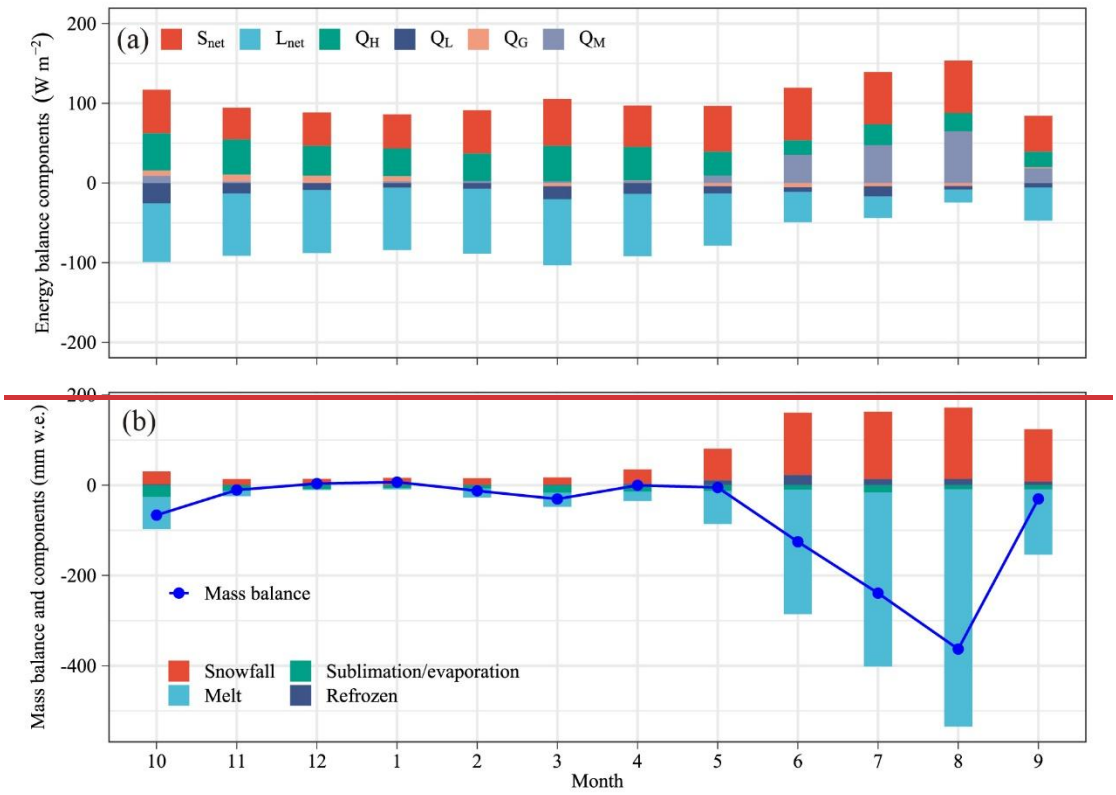
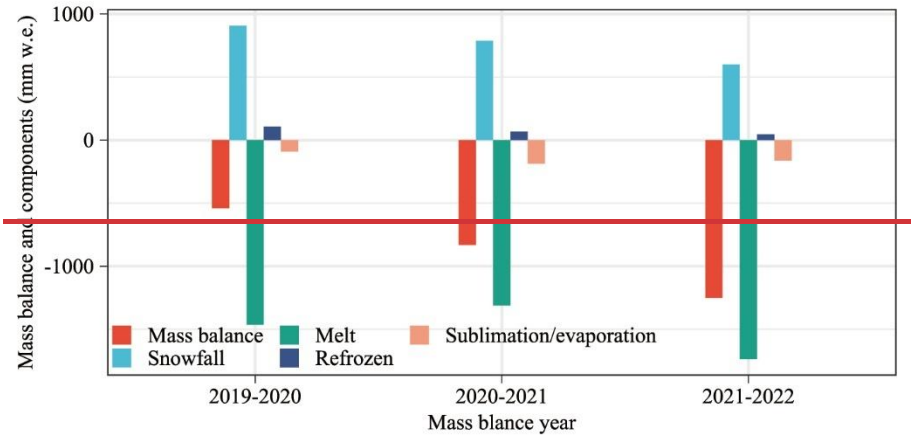


Figure 4. (a) Glacier-wide mean monthly energy and (b) mass fluxes of the energy and mass balance components from October to September during 2019-2022.

The interannual variability of the mass balance and its components was examined. Figure. 5 quantifies glacier-wide fluctuations in mass balance, snowfall, melt, sublimation/evaporation, and refreezing. The 2021-2022 mass balance year emerged as historically exceptional, recording −1 251 mm w.e. - corresponding to 2.3-fold larger magnitude than 2019-2020 (−540 mm w.e.) and 1.5 times that of 2020-2021 (−831 mm w.e.) - representing the most severe deficit since observational records began.

In the central TP, sublimation/evaporation and refreezing typically constitute a small portion of the mass balance, while snowfall and melting account for a larger proportion. The melt exhibits significant interannual variability, ranging from 1464.2 mm w.e. in 2019–2020 to 1736.9 mm w.e. in 2021–2022. Snowfall variability was comparable to sublimation/evaporation, with changes of 307 mm w.e. and 70.6 mm w.e. from 2019–2020 to 2021–2022, respectively. Refreezing shows the smallest variability, ranging from 20.9 mm w.e. to 60.5 mm w.e.. Thus, the interannual variability in the mass balance of Sangqu Glacier was primarily influenced by melting

~~and snowfall during the study period.~~



~~Figure 5. Interannual variation in glacier wide mass balance and its components on Sangqu Glacier in 2019–2020, 2020–2021, and 2021–2022.~~

The seasonal variations in the glacier-wide energy balance and its components during the 2021–2022 mass balance year are presented in Fig 4a. The S_{net} shows significant seasonal variability in the range of 30.2 W m^{-2} to 88.8 W m^{-2}, and this variability is mainly driven by the seasonal shift in the solar elevation angle in conjunction with the glacier surface albedo. L_{net} is the major energy-loss term for the glacier surface energy balance (Fig. 4a). The maximum and minimum values of net longwave radiation are −11.7 W m^{-2} and −87.5 W m^{-2}, which occur in August and March, respectively. The mean L_{net} in the warm and cool seasons are −33.2 W m^{-2} and −76.5 W m^{-2}, respectively. The difference in L_{net} between the warm and cool seasons mainly depends on the difference between L_{in} and L_{out}. In this study, L_{in} is influenced by both air temperature and relative humidity, both of which reach high values in the warm season, corresponding to higher L_{in}. The L_{out} calculated from the glacier surface temperature was also high during the warm season. Combining L_{in} and L_{out}, the absolute value of L_{net} was found to be lower during the warm season than during the cold season. The Q_H on Sangqu Glacier were continuously above 0 W m^{-2} and was an important heat source in the energy balance (Fig. 4a). This indicates that the atmosphere continuously supplies heat to the glacier surface, which helps maintain the glacier surface temperature. The Q_H in the cold and warm seasons are 37 W m^{-2} and 49.4 W m^{-2}, respectively, and this difference may be closely related to the temperature gradient between the glacier surface and the atmosphere, as well as

seasonal changes in wind speed. In contrast, the Q_L on Sangqu Glacier is usually less than 0 W m^{-2}, and the mean Q_L is −21.8 W m^{-2}, indicating that sublimation or evaporation processes are continuously occurring at the glacier surface (Fig. 4a). Q_G depends on the heat transfer coefficients of ice and snow, as well as the temperature gradient (the temperature difference between the surface and the interior of the glacier). The mean Q_G is 0.7 W m^{-2}, indicating that the Q_G accelerates the melting process at the glacier surface (Fig. 4a). Further analysis showed that Q_G in the cold season played an important role in maintaining the energy balance of the glacier surface, whereas in the warm season, it accelerated the melting of the glacier surface. Analysis of the combined energy components reveals that melt energy became positive as early as March, marking the start of ablation on the Sangqu Glacier, with maximum values occurring in July and August (Fig. 4a). This advanced melt onset corroborates the observations of Zhu et al. (2024a). Additionally, melt energy decreases with increasing elevation, reflecting the lower available energy at higher altitudes (Fig. S9).

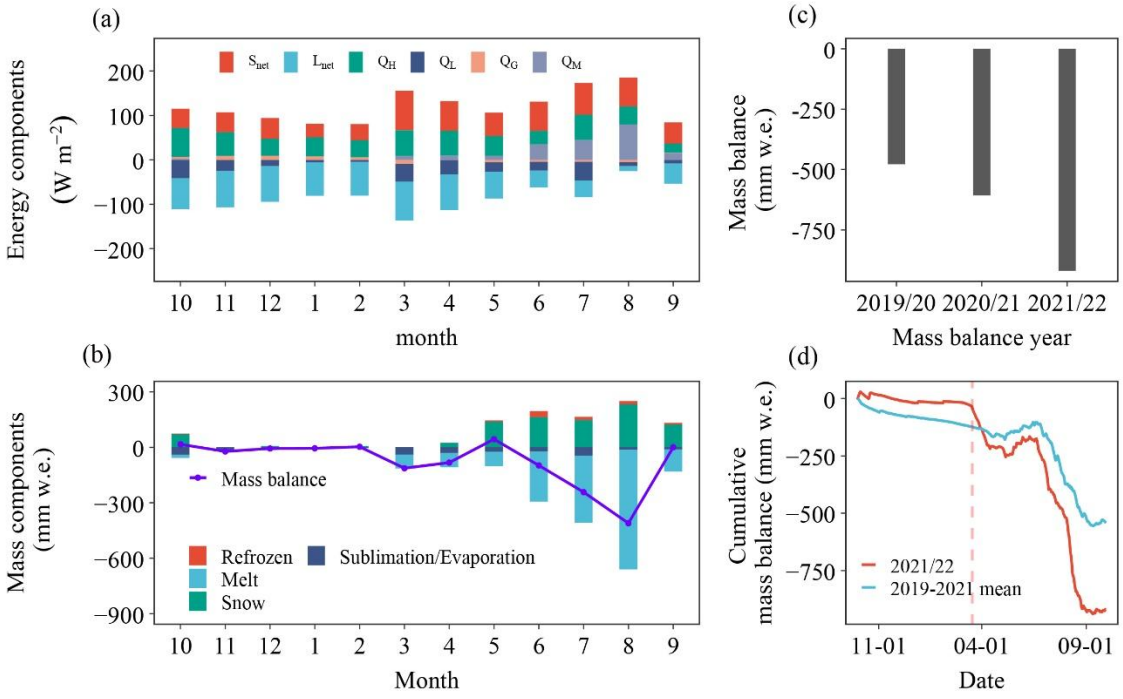


Figure 4. Monthly variations of (a) energy and (b) mass balance components during the 2021–2022 mass balance year. (c) Interannual variations of annual mass balance. (d) Differences in

accumulation mass balance between 2021/22 and the 2019–2021 mean.

The glacier-wide mass balance and its components at the glacial scale are shown in Fig. 4b. Melt, snowfall, refreezing, and sublimation/evaporation are the major mass components of glaciers on central TP.

Mass replenishment comes from snowfall and the refreezing of the snowpack. 73% of snowfall is concentrated in the warm season, and most precipitation falls as snow on glacier surfaces during the warm season. Cold–season snowfall accounts for only 27% of the total snowfall, with less mass replenishment. The total snowfall in April and May, which affects warm–season albedo and glacier melt rates, accounted for 18% of the total snowfall. Meltwater on the glacier surface and water content in the snow are the main sources of mass for refreezing. The volume of refreezing peaks in June, which is related to snow cover and meltwater on the glacier surface. During the observation period, the refreezing amount on Sangqu Glacier accounted for 6% of the melting amount.

The major mass losses from glaciers include melt, sublimation and evaporation. The melt is the dominant component of the mass balance. Melting begins at the glacier surface in March and peaks in July or August, which is related to the seasonal distribution of melt energy. 85% of melt occurs during the warm season. June, July, August, and September account for 16%, 22%, 39%, and 7% of the total melt, respectively. Sublimation/evaporation is a component of the mass balance that cannot be ignored; in this study, sublimation/evaporation on the Sangqu Glacier accounted for 29% of the mass balance.

As illustrated in Fig 4c, the interannual variability in the mass balance of the Sangqu Glacier indicates that mass loss during the 2021/22 mass balance year was substantially more severe than in 2019/20 and 2020/21, surpassing those years by 442 mm w.e. and 312 mm w.e., respectively. Fig 4d shows the anomaly in cumulative mass balance for 2021/22 relative to the 2019–2021 average. This further indicates that the cumulative mass balance in 2021/22 began to diverge negatively from the multi-year average earlier in the year, suggesting an earlier onset of rapid ablation

compared to the two preceding mass balance years.

5.2 Identification and Validation of Extreme Glacier Mass Loss Events on TP

To evaluate the robustness of our proposed dual-threshold framework across different climatic regimes and record lengths, we applied it to five glaciers with long-term mass balance observations on the Tibetan Plateau (Fig. 5 and Fig. S4). Following the methodology described in Sect. 4.4, we first calibrated the multiplier k for each glacier based on the training period. The resulting k_{min} and k_{max} values vary by glacier: for Xiao Dongkemadi Glacier, k_{min} of 1.06 and k_{max} of 1.13; for Qiyi Glacier, k_{min} of 1.28 and k_{max} of 1.34; and for Guliya Glacier, k_{min} of 1.29 and k_{max} of 1.34 (Fig. 5). For Ningchan No. 1 Glacier and Anglong Glacier, the corresponding values are presented in Fig. S4. Using these k values, the relaxed and strict thresholds (as defined in Sect. 4.4) were calculated, enabling the identification of 4–6 extreme mass loss events across the five glaciers. This demonstrates that the framework reliably identifies extreme events even when applied to short-term records.

Given the climatic similarity between Xiao Dongkemadi Glacier and Sangqu Glacier, we applied the k values derived from the former to assess the severity of the 2021/22 mass balance year at Sangqu Glacier. Using the mean and standard deviation of the 2019–2021 mass balance record at Sangqu Glacier, the relaxed and strict thresholds were calculated as –925.1 mm w.e. and –909.2 mm w.e., respectively. The simulated annual mass balance for 2021/22 (–919.8 mm w.e.) falls between these two thresholds, confirming that this mass balance year qualifies as an extreme mass loss event.

This finding is further substantiated by two independent datasets (Hugonnet et al., 2021; Dussaillant et al; 2025). First, satellite-derived glacier mass balance estimates (2000–2019) indicate that the 2021/22 mass loss was approximately twice the annual average for the period 2000–2019 (Fig. S5). Second, global 0.5°-resolution glacier mass balance data (1976–2022) show that the 2021/22 values were 600–700 mm w.e. lower than the 1975–2021 mean (Fig. S6). Collectively, these multi-source datasets provide compelling evidence that the 2021/22 mass loss at Sangqu Glacier was

unprecedented in recent decades.

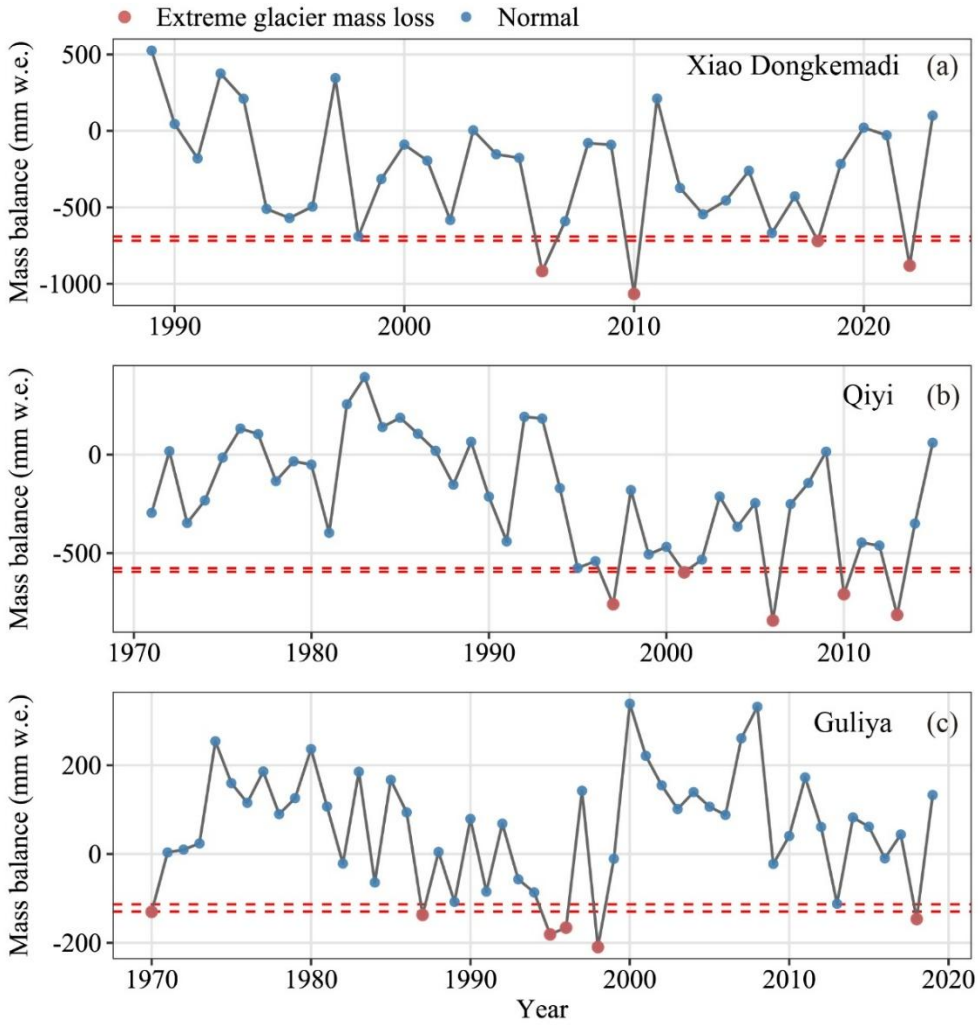


Figure 5. Annual mass balance time series and extreme mass loss events for (a) Xiao Dongkemadi Glacier, (b) Qiyi Glacier, and (c) Guliya Glacier. The data were sourced from Yao et al. (2012), Zhu et al. (2026a) and Zhu et al. (2022a, 2022b). The red dashed line indicates the threshold for identifying extreme mass loss events.

~~5.2 Extreme mass loss and melting event detection~~

~~5.2.1 Identification and Validation of Extreme Glacier Mass Loss Events on TP~~

~~The observed and reconstructed annual mass balance records across TP enable the application of this novel methodology to define critical thresholds for extreme mass loss events. To validate the methodology, we compiled annual mass balance data from five glaciers: Xiao dongkemadi Glacier, Qiyi Glacier, Guliya Glacier, Ningchan No. 1 Glacier, and Anglong Glacier. The derived relaxed and strict thresholds are 1.06 and 1.13 for Xiao dongkemadi Glacier (Figure. 6a), 1.28 and 1.34 for Qiyi Glacier~~

~~(Figure. 6b), and 1.29 and 1.34 for Guliya Glacier (Figure. 6c), respectively. For Ningchan No. 1 Glacier (Figure. S4a) and Anglong Glacier (Figure. S4b), the relaxed thresholds are 1.28 and 1.35, while the strict thresholds are 1.49 and 1.60, respectively. Using this method, we identified 4, 4, and 6 extreme mass loss events in Xiao dongkemadi Glacier (Figure. 6a), Qiyi Glacier (Figure. 6b), and Guliya Glacier (Figure. 6c), respectively. For Ningchan No. 1 Glacier (Figure. S4a) and Anglong Glacier (Figure. S4b), 5 extreme mass loss events were identified in each case.~~

~~Since Xiao dongkemadi Glacier shares similar climate characteristics with Sangqu Glacier, we applied its relaxed (1.06) and strict (1.13) thresholds to calculate critical thresholds for Sangqu Glacier. The resulting thresholds were determined as −1,278 mm w.e. (strict) and −1,252 mm w.e. (relaxed). For the 2021/2022 mass balance year, the calculated value (−1,251 mm w.e.) approached the relaxed threshold (−1,252 mm w.e.) with a 0.08% deviation (Δ=1 mm w.e.), but was 27 mm w.e. less negative than the strict threshold (−1,278 mm w.e.). However, considering the uncertainty bounds (±222.9 mm w.e.), the 2021–2022 mass loss was definitively classified as an extreme event. This conclusion is further supported by two independent datasets: satellite-derived annual averages (2000–2019, Figure. S2) and global 0.5°-resolution glacier mass balance data (1976–2022, Figure. S3), both indicating unprecedented severity. This extreme loss was twice the satellite-derived annual average observed during 2000–2019 (Figure. S2). Furthermore, global 0.5°-resolution glacier mass balance data (1976–2022) indicate that the 2021–2022 values are 600–700 mm w.e. lower than the 1975–2021 mean (Figure. S3).~~

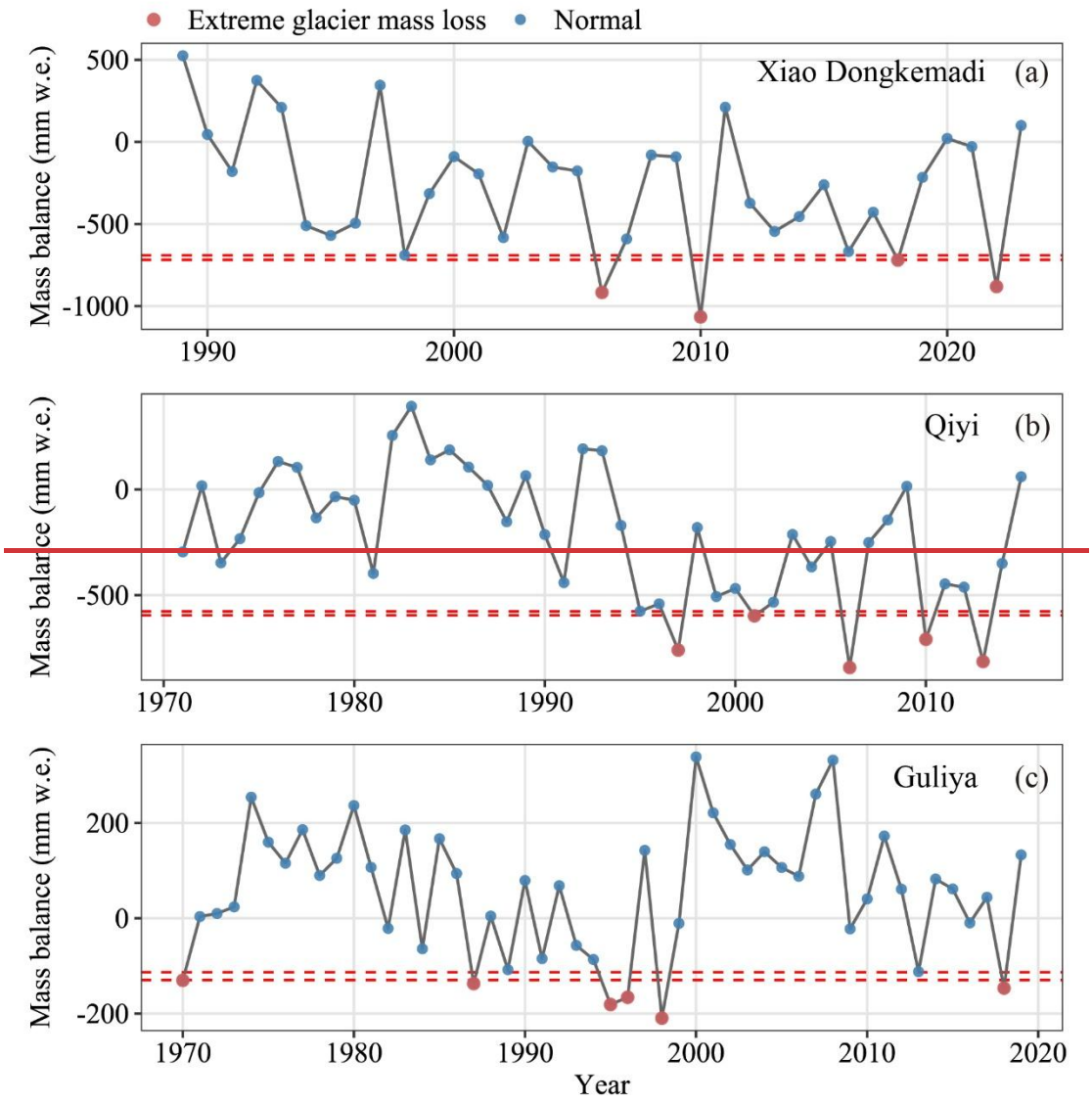


Figure. 6. Annual mass balance time series and extreme mass loss events for (a) Xiao dongkemadi Glacier, (b) Qiyi Glacier, and (c) Guliya Glacier. The data were sourced from Yao et al. (2012), Wei et al. (2025) and Zhu et al. (2022a, 2022b). The red dashed line represents the critical value of *k*.

5.2.2 Detection and Analysis of Extreme Melting Events in the 2022 Summer on Sangqu Glacier

In Section 5.2.1, we identified the 2021–2022 period as an extreme mass loss year. Building on this finding, we further investigated whether summer melt on Sangqu Glacier reached extreme levels during the 2021–2022 mass balance year.

As presented in Section 5.1, our calculations revealed that the melt magnitude for the Sangqu Glacier during 2021–2022 (−1,736.91 mm w.e.) was more negative

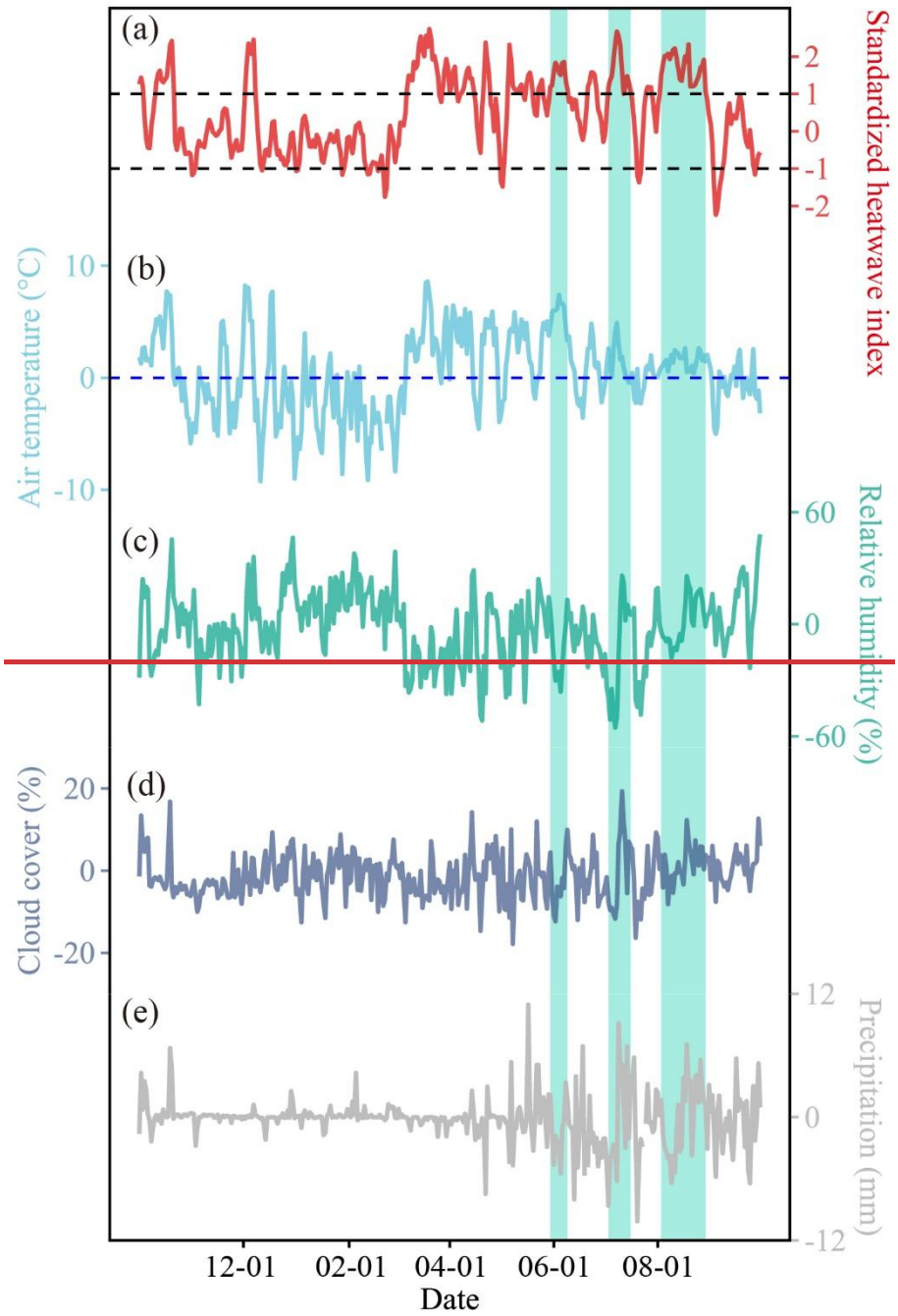
~~compared to the 2019–2020 (−1,464.17 mm w.e.) and 2020–2021 (−1,311.98 mm w.e.) periods. The strict and relaxed melt thresholds (Xiao dongkemadi) calculated using the methodology in Section 4.3 were −1,747.64 mm w.e. and −1,732.57 mm w.e., respectively. Following our classification criteria (Section 4.3), melt values exceeding either the strict or relaxed threshold are considered extreme. Since the 2021–2022 melt value fell between these thresholds (i.e., less negative than the strict threshold (−1,747.64 mm w.e.) but more negative than the relaxed threshold (−1,732.57 mm w.e.)), it was classified as an extreme melt event.~~

~~Air temperature variability is a direct driver of glacier melt, exhibiting a positive correlation with melt intensity. To evaluate whether melt during heatwaves was extreme, we utilized the S_{HI} defined in Section 4.1. The S_{HI}, calculated from long-term daily mean air temperature records (1960–2022) at Tuotuohe National Weather Station, was used to characterize extreme heat events. Based on our criteria ($S_{HI} > 1$ for ≥3 consecutive days), three heatwave periods were identified: 30 May–9 June, 3–16 July, and 3–29 August 2022 (Figure. 7). The associated meteorological anomalies during the heatwave period are shown in Figure 7. The AWS, located at 5,700 m on Sangqu Glacier, exhibited a 2.4 °C positive temperature anomaly alongside a 6.5% reduction in relative humidity during the 2022 summer heatwave events, relative to the 2019–2021 (Figure. 7b and 7c). The cloud fraction was reduced by 26 (50%) during the 52 day of extreme heat waves, with an average reduction of 5.4% (Figure. 7d). Precipitation was reduced by an average of 0.3 mm during extreme heat waves (Figure. 7e). Additionally, compared to the 2019–2021 average melt, a 572 mm w.e. increase in mass loss was observed during the 2022 summer heatwaves. Melt during summer heatwaves exhibited significantly higher frequency and intensity than melt during spring heatwaves (Zhu et al., 2024b), with 52 cumulative summer heatwave days producing 1,135 mm w.e. of melt—accounting for 65.2% of the total 2021–2022 melt (Figure. 7f). From this perspective, glacier melt during the heatwave period may be extreme.~~

~~To empirically validate this hypothesis, we applied the methodology outlined in~~

~~Section 4.3. Our analysis conclusively demonstrated that the 2022 summer heatwaves directly triggered melt conditions that surpassed all documented extremes. The strict and relaxed thresholds for extreme melt during this period were −1,134.47 mm w.e. and −1,110 mm w.e., respectively. The total melt during the 2022 summer heatwaves (−1,134.68 mm w.e.) was more negative than the strict threshold (−1,134.47 mm w.e.), confirming its classification as an extreme event.~~

~~Our analysis demonstrated that the 2021–2022 annual mass balance, annual melt magnitude, and melt driven by summer heatwaves were all classified as extreme events. These results validate the broad applicability of the methodology proposed in Section 4.3 for detecting extreme mass or melt events across diverse temporal and climatic contexts.~~



~~Figure 7. Anomalous meteorological conditions on Sangqu Glacier at 5,700 m during extreme heat waves. (a) standardized heatwave index (S_{HI}). (b) Air temperature (°C), (c) Relative humidity (%), (d) Cloud fraction (%), and (e) Precipitation (mm) anomalies from October 2021 to September 2022 (reference period is October 2019 to September 2021). Color shading represents extreme heat waves.~~

5.3 Surface Energy Balance Responsible for Extreme Melt during summer 2022 heatwave

We conducted a rigorous analysis of the glacier-wide energy balance on Sangqu Glacier during the 2022 summer heatwave, which induced extreme melt. Our results

reveal distinct energy balance anomalies associated with this event, as illustrated in Figs 6 and S7.

Relative to the reference period (October 2019–September 2021), the extreme melt period was characterized by a 2.9 W m^{-2} decrease in S_{in} (Fig. 6a) and an 8.0 W m^{-2} reduction in S_{out} (Fig. S7a). The decline in S_{out} was primarily driven by a 3.5% decrease in albedo (Fig. 6b), resulting in a S_{net} gain of 5.1 W m^{-2} (Fig. S7e). Longwave radiation components also exhibited substantial changes: L_{in} increased by 20.3 W m^{-2} (Fig. 6c), while L_{out} rose by 6.3 W m^{-2} (Fig. S7b). This led to a L_{net} increase of 14.0 W m^{-2} (Fig. S7f). Combined, the increases in S_{net} and L_{net} contributed an additional 19.1 W m^{-2} to the total net radiation.

Regarding turbulent heat fluxes, Q_H showed a marked increase of 17.0 W m^{-2} (Fig. 6d), whereas Q_L decreased by 4.8 W m^{-2} (Fig. S7c). Q_G also declined by 5.0 W m^{-2} (Fig. S7d). These energy balance anomalies substantially enhanced the energy available for melt (Fig. 6e), driven by increased L_{in} and Q_H, alongside reductions in S_{out}, Q_L, and Q_G. The amplified S_{net} resulting from reduced albedo, combined with enhanced L_{in} and Q_H due to warm air advection, ultimately led to the extreme melt during the heatwave. Under these energy balance anomalies, the average melt energy during the heatwave from June to September 2022 increased by 30.7 W m^{-2}, resulting in an exceptional rise in melt amount of 317.8 mm w.e.. The melt amount during this period was 1.66 and 1.69 times that recorded for the same period in 2020 and 2021, respectively.

Current research increasingly identifies energy balance anomalies as the principal driver of extreme glacier melt. Zhu et al. (2024a) demonstrated that early 2022 springtime climatic extremes interacting with anomalous S_{in} and Q_H triggered exceptional melting on Sangqu Glacier. Thibert et al. (2018) reported record melt on Sarennes Glacier (French Alps) controlled by three factors: S_{in} anomalies, Q_L variations, and preseason snowpack conditions. Tian et al. (2023) further established that large-scale circulation patterns modulating cloud cover diurnal cycles induced extreme temperature anomalies in the eastern TP.

Our findings corroborate that energy balance anomalies, characterized by L_{in} enhancement, Q_H amplification, and albedo reduction, were the primary drivers of glacier melt during the 2022 summer heatwave. The observed energy partitioning pattern, featuring synergistic radiative-turbulent flux interactions during these summer extreme events, aligns with documented mechanisms in both Alpine and TP glaciers (Thibert et al., 2018; Zhu et al., 2024a).

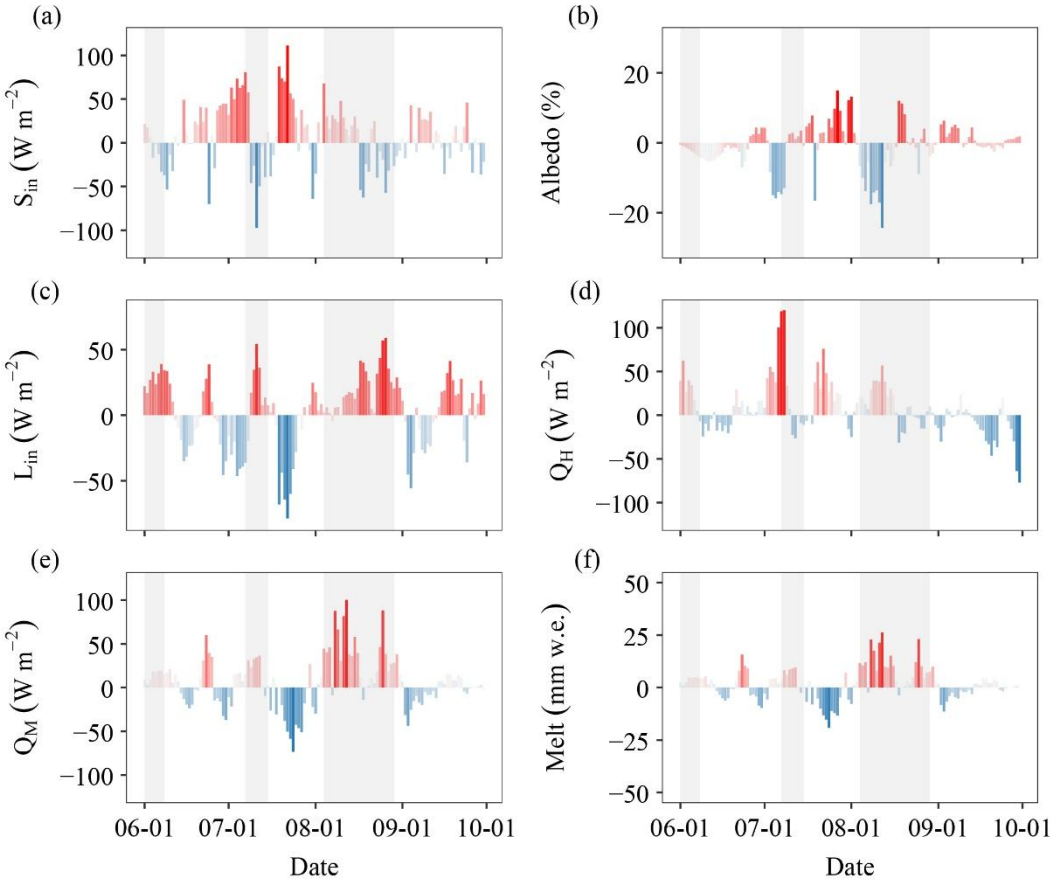


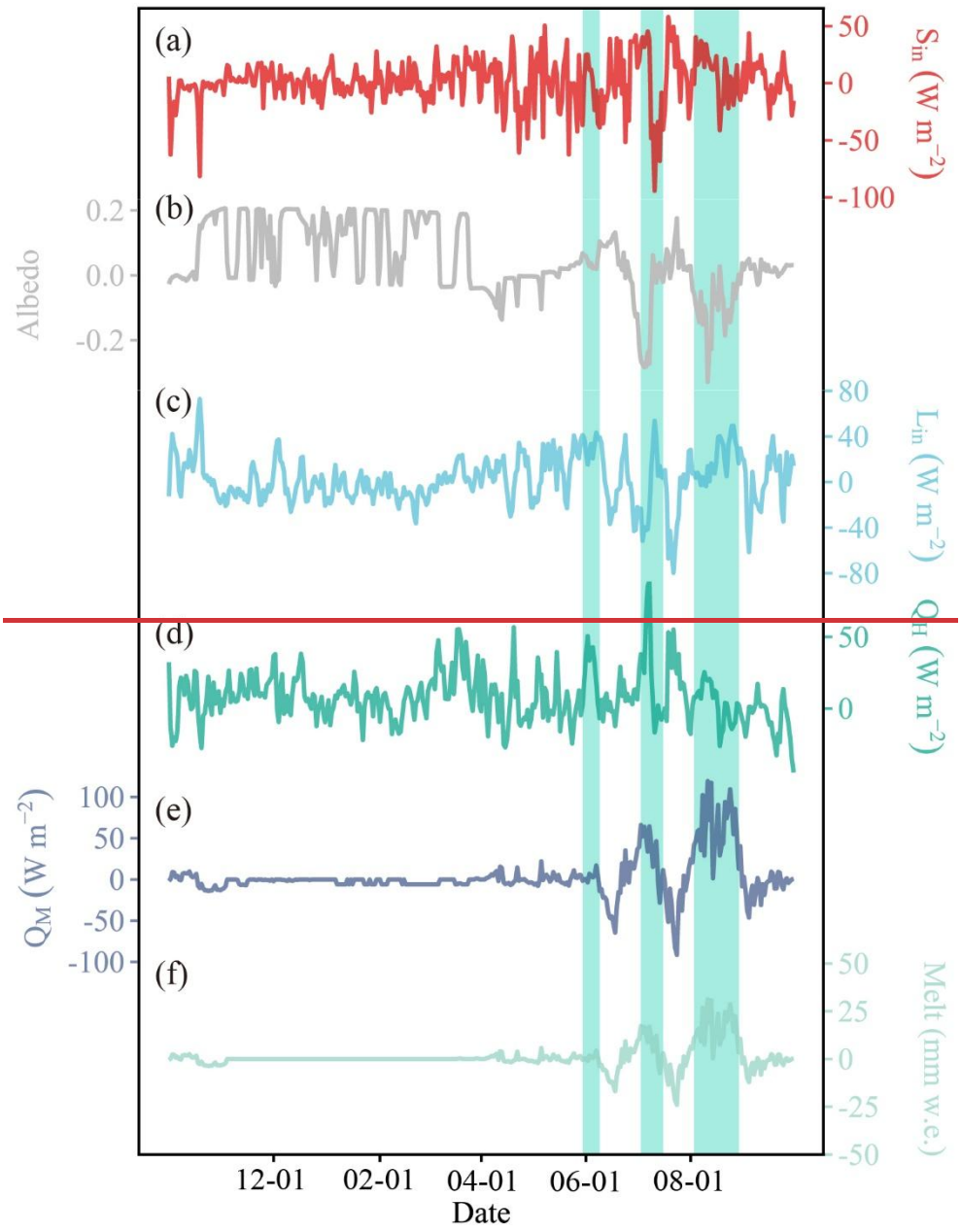
Figure 6. Glacier-wide energy balance anomalies associated with the extreme melt events. Anomalies in (a) incoming shortwave radiation, (b) albedo, (c) incoming longwave radiation, (d) sensible heat flux, (e) melt energy, and (f) melt amount are shown relative to the reference period October 2019–September 2021. Gray shading indicates the 2022 summer heatwave period (June–September).

~~The glacier-wide energy balance during heatwave-induced extreme melt events was rigorously analyzed. Our analysis revealed distinct energy balance anomalies in Sangqu Glacier during extreme heatwaves and melt events, as illustrated in Figure 8 and A2. Compared to the reference period (October 2019-September 2021), the extreme melt period showed a 0.4 W m^{-2} average increase in S_{in} (Figure. 8a) and a~~

~~27.9 W m^{-2} decrease in S_{out} (Figure. A2a), collectively enhancing S_{net} by 28.3 W m^{-2} (Figure. A2e). Longwave radiation components exhibited concurrent changes: L_{in} increased by 15.5 W m^{-2} (Figure. 8c) while L_{out} rose by 4.7 W m^{-2} (Figure. A2b), yielding a L_{net} reduction of 10.8 W m^{-2} (Figure. A2f). The combined S_{out} and L_{net} anomalies produced a 17.5 W m^{-2} increase in net radiative flux. Turbulent heat fluxes demonstrated contrasting trends: Q_H increased by 13.5 W m^{-2} (Figure. 8d), whereas Q_L decreased by 7.4 W m^{-2} (Figure. A2c). Q_G showed a 3.3 W m^{-2} reduction (Figure. A2d). These energy budget perturbations – particularly elevated S_{in}, enhanced L_{in}, and amplified Q_H combined with diminished S_{out}, Q_L, and Q_G – significantly increased melt energy availability (Figure. 8e). The observed 10% albedo reduction (Figure. 8b) suppressed surface reflectance, trapping additional shortwave radiation that synergized with enhanced longwave input and Q_H to drive extreme melt during heatwaves.~~

~~Current research increasingly identifies energy balance anomalies as the principal driver of extreme glacial melt. Zhu et al. (2024b) demonstrated that early 2022 springtime climatic extremes interacting with anomalous S_{in} and Q_H triggered exceptional melting on Sangqu Glacier. Thibert et al. (2018) reported record melt on Sarennes Glacier (French Alps) controlled by three factors: S_{in} anomalies, Q_L variations, and preseason snowpack conditions. Tian et al. (2023) further established that large-scale circulation patterns modulating cloud cover diurnal cycles induced extreme temperature anomalies in the eastern TP.~~

~~Our findings corroborate that energy balance anomalies – characterized by L_{in} enhancement, Q_H amplification, and albedo reduction – primarily drove the 2022 summer heatwave-induced glacier melt. The observed energy partitioning pattern, featuring synergistic radiative-turbulent flux interactions during these summer extreme events, aligns with documented mechanisms in both Alpine and TP glaciers (Thibert et al., 2018; Zhu et al., 2024b).~~



~~Figure 8. Energy balance components associated with the extreme glacier melt events in glacier-wide scale. Anomalous (a) incoming shortwave radiation, (b) albedo, (c) incoming longwave radiation, (d) sensible heat fluxes, (e) melting energy, and (f) melt from October 2021 to October 2022 (reference period is October 2019–September 2021). Color shading represents extreme heat waves.~~

6. Discussion

6.1 Effects of Atmospheric Circulation on Extreme Glacier Melt and heat waves

A growing body of research indicates that large-scale circulation anomalies influence glacier mass balance over the Tibetan Plateau and its surrounding regions by modulating temperature and precipitation patterns (Yao et al., 2012). Specific

configurations of these anomalies, particularly those leading to extreme high-temperature events, have had marked impacts on glacier mass balance in the region. Previous studies have identified the Western Pacific subtropical high, the South Asian high, and the westerly circulation as the primary large-scale systems affecting the plateau. This study finds that during the 2022 summer heatwave, the Western Pacific subtropical high exhibited a pronounced westward extension relative to its climatological mean (Fig. 7b), while the South Asian high extended anomalously eastward (Fig. 7a). Additionally, the meridional displacement of the westerly jet stream played a crucial role, as captured by the subtropical westerly jet (SWJ index) defined as the first principal component of an empirical orthogonal function (EOF) analysis of 200 hPa zonal winds over the region 20°N–50°N, 40°E–90°E (Wei and Yu, 2024). The spatial pattern of the first EOF mode shows positive anomalies between 40°N and 50°N and negative anomalies between 25°N and 35°N, indicating a northward shift of the westerly circulation during the 2022 summer heatwave (Fig. 7c). Time series analysis further supports this northward displacement, with the SWJ index exhibiting a sustained positive phase over the same period (Fig. 7d).

Subsequent studies have reinforced the role of anomalies in the Western Pacific subtropical high, South Asian high, and westerly circulation in driving extreme high temperatures over the TP. Zhou et al. (2024) found that in the summer of 2022, the Western Pacific subtropical high extended anomalously westward, while the Iranian high extended northeastward. Concurrently, an expanded influence of the South Asian high subjected the plateau to a barotropic high-pressure system. This circulation configuration, accompanied by a northward shift of the subtropical westerly jet, reduced moisture transport toward the TP (Wang et al., 2017).

These large-scale circulation anomalies also produced significant local effects. During the summer heatwave, increased cloud cover (Fig. S10b) and a substantial rise in downward longwave radiation (Fig. S10c) contributed to elevated air temperatures (Fig. S10a). This warming was accompanied by increased soil temperatures (Fig. S10e) and decreased soil moisture due to enhanced evaporation (Fig. S10f). The

resulting dry soil conditions are not merely a passive response to atmospheric forcing but can feedback onto the circulation system. Jiang et al. (2024) suggest that soil drought over the TP can further sustain and even intensify the northward shift of the subtropical westerly jet by exciting quasi-stationary Rossby waves. Furthermore, the drier surface enhances the upward sensible heat flux (Fig. S10d), which warms the mid-to-upper troposphere, providing favorable local thermodynamic conditions for the maintenance of the barotropic high-pressure system and the persistence of the heatwave.

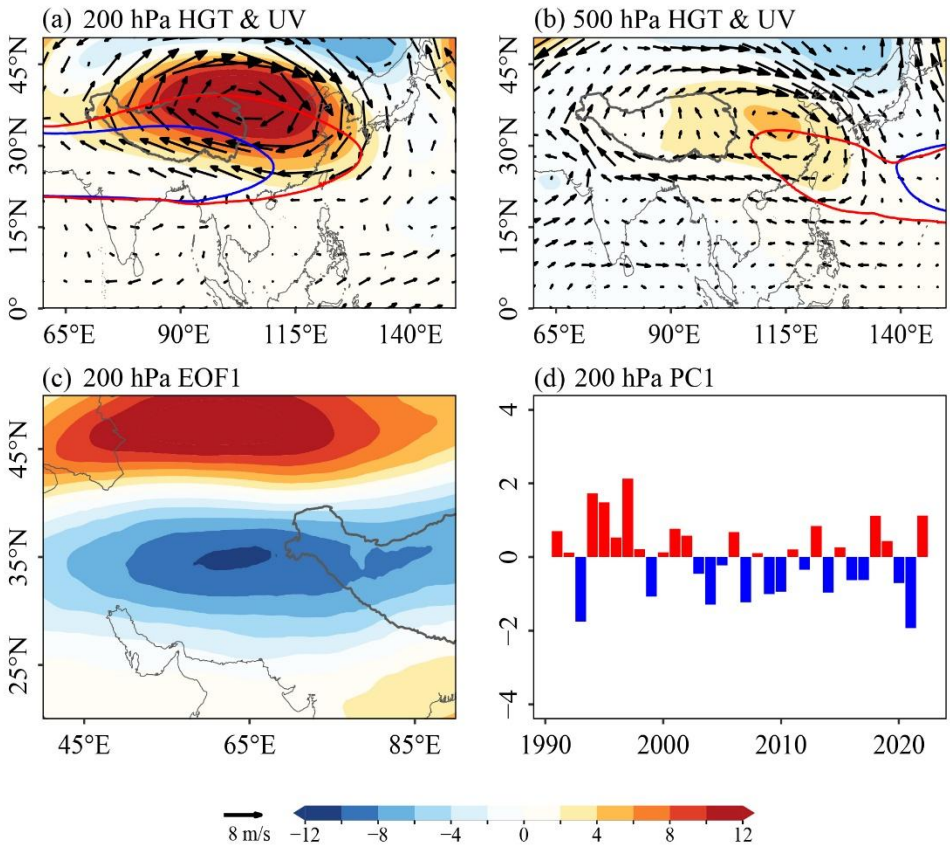


Figure 7. Atmospheric circulation anomalies and dominant modes during the 2022 summer heatwave. Anomalies are calculated relative to the 1992–2021 climatology. (a, b) Spatial distribution of geopotential height (shading) and horizontal wind (vectors) at (a) 200 hPa and (b) 500 hPa during the 2022 summer heatwave. (c) The first leading EOF mode of 200 hPa zonal wind anomalies averaged over the same calendar periods as the 2022 heatwave (1–8 June, 7–15 July, and 4–29 August) for each year from 1991 to 2022, over the region (20°–50°N, 40°–90°E). (d) The corresponding normalized principal component (PC1) time series for 1991–2022. The blue solid (dashed) contour in (a) represents the 1250 gpm isopleth at 200 hPa. The blue solid (dashed) contour in (b) represents the 5880 gpm isopleth at 500 hPa.

~~An increasing body of research has demonstrated that large-scale circulation~~

~~anomalies govern variations in glacier mass balance across TP and adjacent regions through their modulation of both air temperature and precipitation patterns (Yao et al., 2012). In this study, we provide evidence that atmospheric circulation anomalies constituted the primary driver of the unprecedented glacier melt observed during the 2022 summer heatwave events.~~

~~During the initial phase of extreme melting (30 May to 9 June 2022; Figure. 9a and 9d), a vertically stacked anticyclonic anomaly system prevailed over the Sangqu Glacier region. At 200 hPa, the glacier was positioned directly under the core of a TP-centered anticyclonic anomaly. Concurrently at 500 hPa, Mongolian and western Pacific anticyclonic anomalies emerged northeast and east of the glacier, respectively. This multi-level atmospheric configuration generated anomalously intensified easterlies penetrating into the central TP compared to climatological norms. Crucially, the combined effects of these anticyclonic systems – including the northward-displaced SAH and westward-extended WPSH – synergistically induced extreme air temperature anomalies while amplifying glacier melt through enhanced diabatic heating.~~

~~The second phase (3-16 July 2022) was characterized by contrasting positional anomalies of the SAH and WPSH relative to climatological baselines (Figure. 9b and 9e). Although anticyclonic anomalies persisted over TP, the SAH exhibited eastward displacement while the WPSH underwent significant westward expansion. This dipole configuration enhanced moisture convergence and intensified subsidence-driven radiative heating over the glacier surface. The synergistic interaction between these atmospheric systems amplified diabatic heating processes, leading to accelerated surface melt rates during this phase.~~

~~During the third phase (3-29 August 2022; Figure. 9c and 9f), a vertically stratified anticyclonic anomaly system developed with three-dimensional coherence. At 200 hPa, the anticyclonic anomaly center migrated northeast of Sangqu Glacier, coinciding with an exceptionally eastward-extended SAH spanning from TP to eastern China. Concurrently at 500 hPa, the westward-expanded WPSH stretched from the~~

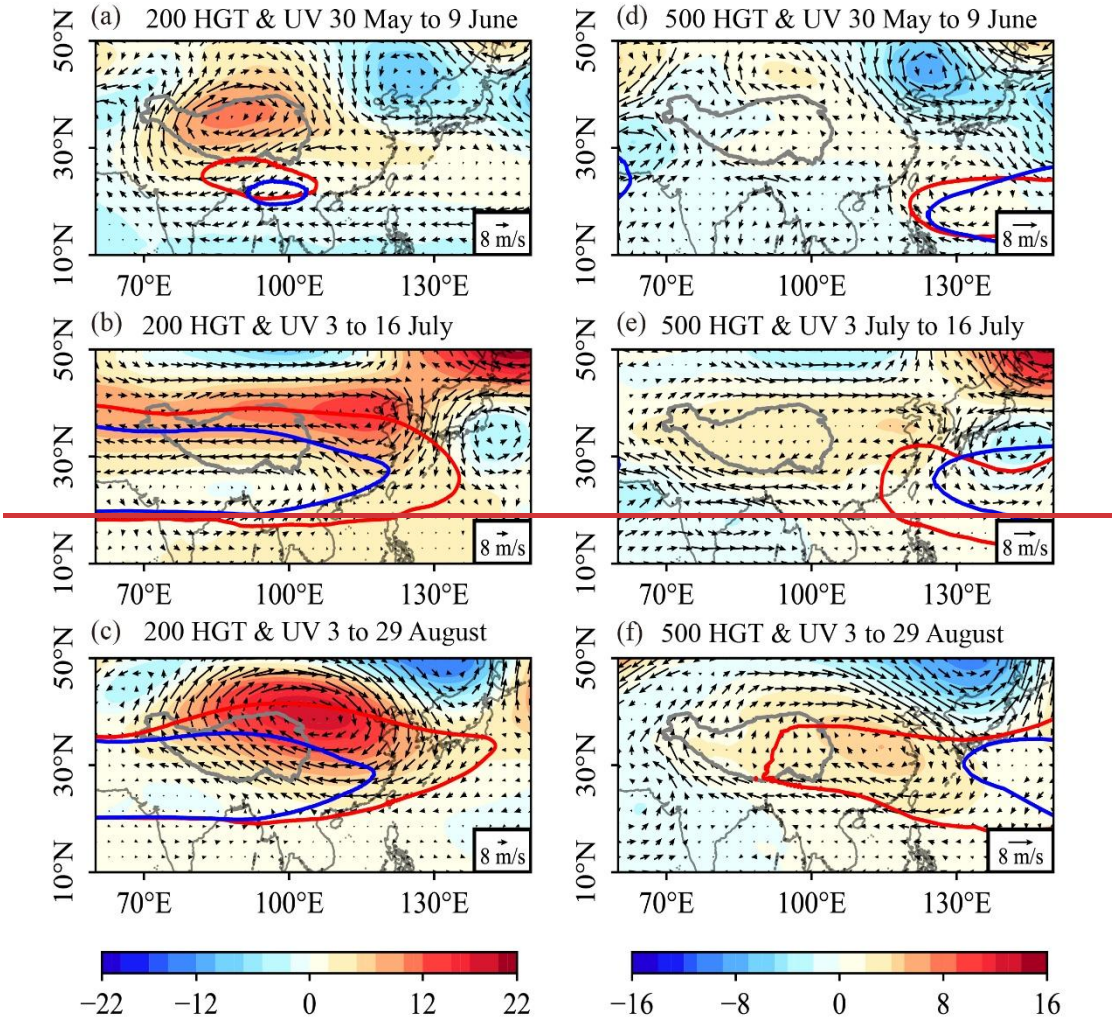
~~western Pacific to eastern China and the central TP, establishing a stable anticyclonic regime east of the glacier. This multi-layered configuration enhanced persistent warm advection thermodynamically while suppressing cloud cover, collectively contributing to the seasonally prolonged and thermally extreme melt episode.~~

~~Convergent evidence from recent studies confirms that large-scale circulation anomalies critically drove the 2022 summer heatwaves across TP and eastern China. Previous work has identified that quasi-stationary high-pressure anomalies, combined with anomalous descending motions and enhanced shortwave radiation, were key drivers of both: (1) the extreme summer 2022 heatwave in central China (Hua et al., 2023; Chen & Li, 2023), and (2) the early-spring 2022 glacier melt and heatwave in the central TP (Zhu et al., 2024b).~~

~~The 2022 summer saw an intensified and westward-extended WPSH coupled with an eastward-extended SAH, which jointly maintained persistent high-pressure anomalies over central-eastern TP (Zhou et al., 2024). Vertical overlap between the WPSH and SAH further reinforced these anomalies, prolonging heatwaves in the region (Li et al., 2021). These circulation patterns corresponded to elevated air temperatures alongside reduced precipitation and cloud cover across central-eastern TP during June-September 2022. The associated descending motions reduced cloudiness, allowing intensified surface shortwave radiation that heated the land (Hua et al., 2023). This warming triggered local soil-atmosphere feedbacks, with enhanced sensible heat flux and longwave radiation further energizing the atmospheric column (Jiang et al., 2023). The synergy of these thermodynamic processes culminated in extreme air temperatures and accelerated glacier melt throughout the 2022 summer in central-eastern TP.~~

~~The persistent TP anticyclone elevated air temperatures while suppressing precipitation across the central-western TP. The vertical overlap of the WPSH and SAH critically disrupted water vapor transport toward the central TP. This high-pressure regime further suppressed convective activity spanning from the Himalayas to southeastern and central TP, exacerbating regional precipitation deficits.~~

~~Under these sustained anticyclonic conditions, a distinct moisture circulation anomaly with anticyclonic flow developed over the southwestern TP (Figure. 10). Weakened northwestward and northeastward moisture transport from the Indian Ocean and Arabian Sea induced pronounced moisture divergence over the central-western TP. Coupled with persistent anticyclonic forcing, these circulation dynamics collectively drove the observed precipitation reduction in the central TP during the 2022 heatwave.~~



~~Figure 9. Spatial distribution of the geopotential height (shading) and horizontal wind (vector) at (a-c) (200 hPa) and (e-f) (500 hPa). The blue solid (dashed) contour in (a), (c) and (e) represents the 1250 gpm isopleth at the 200 hPa. The blue solid (dashed) contour in (b), (d) and (f) represents the 5880 gpm isopleth at the 500 hPa.~~

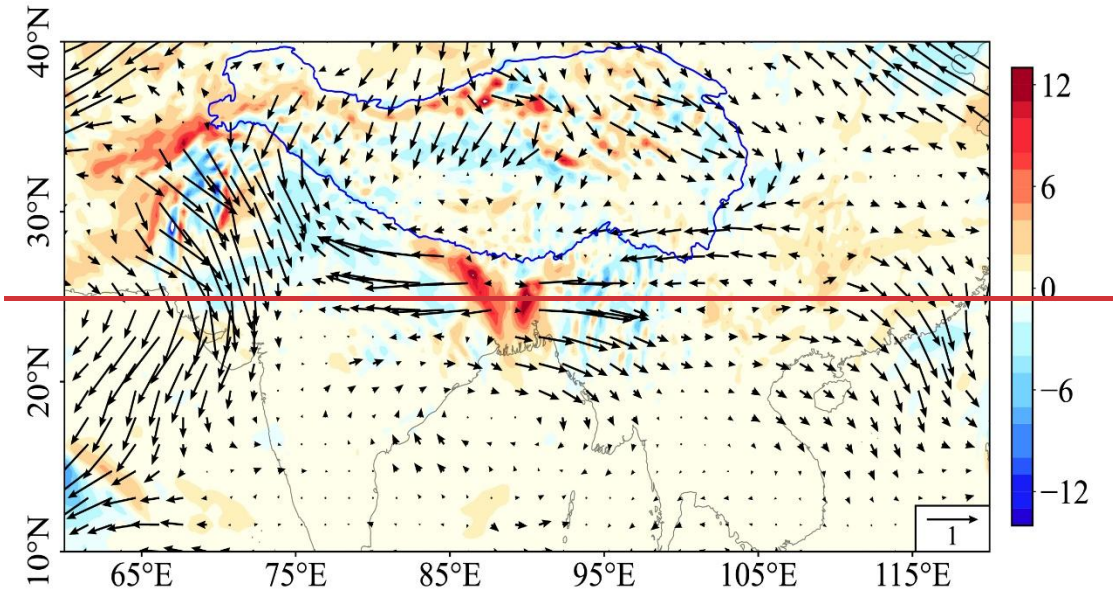


Figure 10. Spatial distribution of the vertically integrated water vapour flux (kg m^{-1} s^{-1}) and its divergence (shading; 10^{-5} kg·m^{-2} s^{-1}) anomalies during the three summer 2022 heatwave events.

Current studies have also examined drivers of the 2022 summer precipitation deficit over TP and eastern China from alternative perspectives. For instance, anomalous spring TP warming, associated with reduced snow cover, has been linked to the northeastward displacement of the SAH and northwestward migration of the WPSH (Li et al., 2023). Concurrently, this preseason warming weakened the southwest monsoon originating from the Bay of Bengal, enhanced the east–west sea surface temperature gradient in the Indian Ocean, and generated anomalous easterly winds along Indonesia's western coast (Cai et al., 2023).

Additionally, Antarctic warm anomalies shifted the Asian monsoon circulation southward, promoting water vapor convergence over Pakistan (Zhang et al., 2024). Jeong et al. (2023) further demonstrated that the co-occurrence of a negative Indian Ocean Dipole and La Niña during summer 2022 amplified rainfall in the northwestern Indian subcontinent and Pakistan while suppressing precipitation in southern China and the central TP. Collectively, interactions between large-scale circulation patterns and regional atmospheric anomalies drove the prolonged high temperatures, low precipitation and extreme melt events observed across the central TP from June to September 2022.

Recent studies have further investigated contributing factors to the 2022 summer precipitation deficit across TP and eastern China through complementary approaches. Spring TP warming anomalies - associated with diminished snow cover - have been shown to displace the SAH northeastward and shift the WPSH northwestward (Li et al., 2023). This preseason thermal anomaly concurrently weakened the Bay of Bengal-originating southwest monsoon, intensified the Indian Ocean's zonal sea surface temperature gradient, and generated anomalous easterlies along Indonesia's western coast (Cai et al., 2023). Antarctic thermal anomalies induced a southward meridional shift in Asian monsoon circulation, enhancing water vapor convergence over Pakistan (Zhang et al., 2024a). Jeong et al. (2023) established that the concurrent 2022 summer negative Indian Ocean Dipole and La Niña conditions amplified rainfall across the northwestern Indian subcontinent and Pakistan, while strongly suppressing precipitation in southern China and central TP.

The synergistic interplay between hemispheric-scale circulation patterns and regional atmospheric anomalies ultimately drove the extended period of elevated air temperatures, precipitation deficits, and extreme melt events observed across central TP from June to September 2022.

6.2 Hydrological Effects of Extreme Heatwaves and Glacial Melt Events

Extreme heatwaves and associated melting events significantly alter hydrological regimes in glacier-fed basins, triggering anomalous runoff surges and flood risks such as increased flood hazards. The seasonal occurrence of heatwaves influences ice-snow melting intensity and regulates meltwater contributions to total runoff through albedo-melt feedback mechanisms. Hydrological analyses reveal that glacial meltwater contributions to total runoff during 2022 heatwaves substantially exceeded baseline summer levels observed from 2019 to 2021 (Zhu et al., 2024a). The early-season heatwave (May 30 to June 9) initiated crucial cryosphere transformations: rapid snowpack depletion exposed underlying glacier ice, which lowered surface albedo and increased radiative energy absorption. These surface alterations prolonged albedo-melt feedback processes that interacted synergistically with subsequent July-

~~August heatwaves, resulting in cumulative melt amplification effects. Furthermore, the early-season heatwave accelerated the timing of snowmelt, diminishing the snowpack's capacity to sustain total runoff while potentially leading to seasonal drought conditions (Anderson et al., 2023). This dual impact - combining intensified glacier melt with reduced non-glacier snowpack contributions - fundamentally transformed basin-scale water budgets throughout June to September in the summer of 2022.~~

6.2 Comparison with extreme glacier mass loss events in other regions during 2021–2022

In recent years, investigations conducted in diverse mountain glacier regions across the globe have examined extreme mass loss events. These regions include Switzerland (Van Tiel et al., 2026), Austria (Voordendag et al., 2023), the Arctic Svalbard (Bernard and Friedt, 2025), the Pyrenees (Izagirre et al., 2024), the Tien Shan in China (Xu et al., 2024), western Canada and the United States (Menounos et al., 2025), the central TP (Zhu et al., 2024a), and New Zealand (Vargo et al., 2020). These studies have revealed common characteristics and driving mechanisms underlying such events. The distinctive features include record ablation rates and rapid glacier state degradation. In the Swiss Alps, glacier mass loss in 2022 was more than triple the 1991–2020 average, with summer melt intensity breaking observational records. In basins with 15% glacier cover, this summer ice melt compensated for precipitation and snowmelt deficits (Van Tiel et al., 2026). In the Pyrenees, glacier area shrank by nearly 40% between 2020 and 2023, with thinning rates more than three times those of the previous decade (Izagirre et al., 2024). Urumqi Glacier No. 1 in the Tien Shan also recorded severe mass loss in 2022 (Xu et al., 2024). Glaciers on the central Tibetan Plateau experienced anomalous melting in early spring, a season typically considered part of the accumulation period (Zhu et al., 2024a). In western Canada and the United States, mass loss rates between 2021 and 2024 doubled relative to 2010–2020, cumulatively reducing glacier mass by 12% (Menounos et al., 2025).

The mechanisms driving these extreme mass loss events involve multiple interacting factors. First, anomalous large-scale atmospheric circulation provided the background conditions for extreme weather and climate events. The weakening and northward shift of the mid-latitude westerly jet stream, for instance, disrupted cold moist air transport to the TP, leading to persistent high temperatures (Zhu et al., 2024a). Second, record-breaking summer heatwaves superimposed on deficient winter snowfall directly supplied substantial energy for glacier melt (Menounos et al., 2025; Xu et al., 2024). From an energy balance perspective, this anomaly manifested as significant increases in incoming shortwave radiation due to reduced cloud cover and in sensible heat flux. On Sarennes Glacier in the French Alps, for example, the extreme melt in 2003 was dominated by a substantial increase in global radiation and sensible heat flux (Thibert et al., 2018). Finally, a key accelerating mechanism is the albedo feedback on glacier surfaces: high temperatures lead to earlier snowmelt, exposing lower-albedo ice. The deposition of black carbon from wildfires in North America or Saharan dust in the Alps further reduces albedo, causing the glacier to absorb more solar radiation and thereby establishing a feedback loop that amplifies melting (Menounos et al., 2025; Van Tiel et al., 2026). Event attribution studies in New Zealand have confirmed that anthropogenic warming made extreme mass loss years like 2011 and 2018 at least six to ten times more likely (Vargo et al., 2020). Research on Austre Lovénbreen in the Arctic revealed that a heatwave and liquid precipitation event in March 2022 altered snowpack structure, significantly advancing glacier ice exposure and prolonging the melt season. This represents another crucial mechanism exacerbating mass loss (Bernard and Friedt, 2025). In the same year at Hintereisferner in Austria, extremely low winter accumulation, 43% below the 2011–2020 average, combined with an early melt season onset to advance the Glacier Loss Day to 23 June, 49 days earlier than normal. This ultimately resulted in annual mass loss 3.2 times the 1991–2020 average (Voordendag et al., 2023). These extreme glacier mass loss events are driven by a combination of interacting mechanisms. Anomalous atmospheric circulation patterns and record-breaking heatwaves provide

the energy background, while winter snow deficits, snowpack destabilization induced by liquid precipitation, and albedo feedback collectively lead to earlier glacier ice exposure and a prolonged melt season, thereby synergistically intensifying glacier ablation.

Therefore, glaciers across global mountain regions during 2021–2022 exhibited common characteristics of extreme mass loss, including record-breaking ablation rates, accelerated area shrinkage and thinning, and a short-term hydrological buffering effect that compensated for precipitation deficits. These extreme melt events were driven synergistically by anomalous large-scale atmospheric circulation and record summer heatwaves, amplified by mechanisms such as winter snow deficits, liquid precipitation-induced snowpack destabilization, and surface albedo feedback, underscoring the need for systematic research on more frequent extreme events.

6.3 Implications of Extreme Heatwaves and Glacier Melt Events for Hydrological Processes

In glacier-fed basins, extreme weather and climate events, such as extreme heat, drought, and heavy precipitation, strongly influence glacier melt and hydrological processes. Research across the Arctic (Boon et al., 2003), Greenland (Kondo et al., 2021), the Canadian Rockies (Anderson and Radić, 2023), the European Alps (Koboltschnig et al., 2009; Koboltschnig and Schöner, 2011; Van Tiel et al., 2026), and the TP (Zhu et al., 2024b) shows that extreme heat-driven melt events affect basin runoff across three timescales: short-term hazards, seasonal water allocation, and long-term trends.

On short timescales, extreme heat intensifies turbulent heat fluxes and triggers albedo feedback, causing melt rates and runoff to surge within days. Studies from the High Arctic (Boon et al., 2003), Greenland (Kondo et al., 2021), and the European Alps (Koboltschnig et al., 2009) document that such events can produce large fractions of seasonal ablation in just a few days or generate flash floods when combined with strong winds.

At the seasonal scale, extreme melt events alter the timing and composition of

runoff. Spring heatwaves often cause early snow depletion, leading to runoff deficits later in the season. In glacierized basins, sustained summer melt can partially offset these deficits, whereas non-glacierized basins experience sharp declines (Anderson and Radić, 2023). Evidence from Austria and the TP further shows that during extreme heatwaves (Koboltschnig and Schöner, 2011; Zhu et al., 2024b), glacier melt contributions can increase even when total runoff drops, a pattern linked to albedo feedback, which consistently amplifies melt across different climatic regions.

Over the long term, however, this buffering capacity is weakening. Despite record-high summer temperatures and melt rates, total meltwater volumes have declined in recent extreme years due to glacier area loss, indicating that continued glacier shrinkage can offset the effect of even extreme heat (Van Tiel et al., 2026).

Taken together, these findings highlight that the response of glacierized basins to extreme heat is shaped by thermal forcing, glacier characteristics (such as snowline, bare ice extent, and ice volume), and long-term climate change. Current evidence suggests a shift from a linear melt response to a nonlinear phase, characterized by rising short-term flood risks, declining long-term water supply, and fundamental changes in runoff composition.

6.4 Research Limitations

While this study integrates multi-source data with an energy-mass balance model to reveal the extreme melting processes and mechanisms of the Sangqu Glacier on the central TP driven by the 2022 summer heatwave, several limitations warrant further investigation.

The AWS was deployed at only a single elevation point on the glacier surface, resulting in spatiotemporal gaps that make spatial extrapolation of meteorological variables a primary source of model uncertainty. We used parameterization schemes such as temperature lapse rates and precipitation gradients to extrapolate point-scale observations to the entire glacier and conducted sensitivity analyses. However, this simplified approach cannot fully capture the spatiotemporal heterogeneity of meteorological variables under complex terrain conditions, which may introduce

uncertainty especially during extreme weather and climate events. Other studies have also indicated that even with physically robust energy balance models, spatial extrapolation of meteorological variables remains a major source of model uncertainty requiring multi-source data constraints (Kinnard et al., 2022). Moreover, logistical challenges on the TP, such as power failures and harsh environmental conditions, persistently hamper field data continuity. We used observational data as much as possible to constrain the model and employed mass balance observations from the adjacent Xiao Dongkemadi Glacier (2021/22) for independent validation, yet these data gaps inevitably affect the precision of interannual comparisons.

We did not apply explicit seasonal bias correction to the downscaled ERA5 data. However, validation for the ablation season (Fig. S8) shows good agreement with observations, suggesting minimal seasonal bias during summer. Nevertheless, this simplification may introduce uncertainties under extreme conditions and should be addressed in future work. Additionally, while we used a random forest method to statistically downscale ERA5 reanalysis data, the inherent errors of the downscaling model were not incorporated into the final uncertainty assessment, a factor that could be significant under extreme climatic anomalies.

While the EBFM performs well at the glacier-wide scale, discrepancies are evident at finer scales (point and seasonal), reflecting inherent challenges of distributed glacier modeling under data-scarce conditions. These deviations arise from spatial extrapolation of meteorological variables using simplified lapse rates and gradients, parameterization uncertainty (with albedo and temperature lapse rate being the most sensitive parameters), scale mismatch between point stakes and grid-cell averages, and observational uncertainties in density assumptions and stake height readings. Despite these limitations, the model's accuracy at the glacier-wide scale is sufficient for our extreme event analysis, and independent verification from the neighboring Xiao Dongkemadi Glacier supports the reliability of our conclusions.

The EBFM employed in this study has been validated at multiple scales, but its calibration of key parameters, including snow/ice albedo, turbulent exchange

coefficients, and precipitation gradients, relies on limited observational data. This introduces uncertainties in the key parameterization schemes and may affect the model's extrapolation capability under extreme conditions. Studies in other regions have shown that different combinations of parameterization schemes can lead to considerable differences in the simulated individual energy flux components while having a relatively smaller impact on total melting energy, suggesting that total melt is less sensitive to different parameterization schemes than the individual flux components themselves (Draeger et al., 2024). This finding is consistent with the results of our sensitivity analysis. Nevertheless, our uncertainty assessment through parameter perturbation may still not fully capture the nonlinearities inherent in heatwave-driven processes. Additionally, the model does not account for snow redistribution processes such as wind-driven transport and avalanches, which may influence the spatial distribution of mass balance, particularly in complex terrain.

A simplification in this study is the assumption of fixed glacier geometry, which neglects the feedback effects of glacier thinning and area retreat on mass balance. This feedback is inherently nonlinear: surface elevation lowering leads to higher air temperatures, while glacier terminus retreat can alter local precipitation patterns. Particularly during extreme melt years, rapid changes in glacier geometry can modify the local energy budget, and neglecting this process may bias melt magnitude estimates. For instance, Bolibar et al. (2022) demonstrated that topographic feedback resulting from glacier retreat to higher elevations can partially compensate for the negative impacts of climatic warming on mass balance, whereas a fixed-geometry assumption tends to overestimate melt sensitivity. More critically, the fixed-geometry assumption limits our understanding of the evolution of total glacier melt. As shown by Van Tiel et al. (2026) in the Swiss Alps, the reduction in glacier area can eventually supersede enhanced melt rates as the dominant driver of total discharge. Therefore, future research should couple energy-balance models with ice dynamics and incorporate multi-temporal glacier boundary data to better resolve the transient response of glacier mass balance to extreme climate conditions and its downstream

hydrological impacts.

This study focused on Sangqu Glacier on the central TP, which is situated at the confluence of the mid-latitude westerlies and the Indian monsoon. Consequently, the regional generalizability of our findings requires broader validation. Glacier sensitivity to climatic anomalies varies markedly across the TP, from the humid southeast to the arid northwest (Yao et al., 2012; Zhu et al., 2018). Whether the extreme melting mechanism identified here, driven by enhanced sensible heat flux, increased downward longwave radiation, and reduced albedo, can be directly extended to other glacier types remains to be examined through similar studies in more representative sub-regions. Future research should strengthen multi-glacier collaborative observation networks and integrate high-resolution regional climate modeling to deepen our understanding of extreme melt mechanisms across diverse climatic regimes.

7. Conclusion

~~In this study, we combined multi-source data (October 2019 to September 2022) with a surface energy-mass balance model and a novel dual-threshold framework to identify extreme mass loss events in short-term glacier mass balance records on Sangqu Glacier, enabling a three-year analysis of energy-mass balance characteristics and melt mechanisms during heatwave events in the Geladandong region of the central Tibetan Plateau.~~

~~The EBFM can better capture the energy and mass balance processes of Sangqu Glacier. Measured and simulated values of albedo, incoming shortwave radiation, incoming/outgoing longwave radiation, point mass balance, and glacier-wide mass balance across elevations were in strong agreement. The energy and mass balances on the glacier surface are characterized by significant seasonal and interannual variations. Net shortwave and longwave radiation are the most important components of energy balance. Glacier surface energy and mass balances exhibit pronounced seasonal and interannual variability. Annual surface mass balance values for 2019–2020 (−540 mm w.e.) and 2020–2021 (−831 mm w.e.) contrast sharply with the~~

~~extreme deficit of −1251 mm w.e. in 2021–2022, marking the most severe mass loss in the study period. Our dual-threshold detection method conclusively identified the extreme mass loss event at Sangqu Glacier, demonstrating its robustness in short-record contexts.~~

~~Compared to the 2019–2021 average melt, a 572 mm w.e. increase in mass loss was observed during the 2022 summer heatwaves. Melt during summer heatwaves exhibited significantly higher frequency and intensity than melt during spring heatwaves (Zhu et al., 2024b), with 52 cumulative summer heatwave days producing 1,135 mm w.e. of melt—accounting for 65.2% of the total 2021–2022 melt. These melt events are associated with anomalously low albedo, high incoming longwave radiation, and sensible heat fluxes. Such anomalies in the energy balance were driven by large-scale atmospheric circulation anomalies: specifically, the concurrent intensification and westward expansion of the Western Pacific Subtropical High (WPSH) and the eastward extension of the South Asian High (SAH). This atmospheric circulation anomaly pattern induced high air temperatures via anticyclonic subsidence while causing reduced precipitation through suppressed moisture transport. Future research should extend the dual-threshold framework to other TP glaciers to evaluate its efficacy in detecting extreme melt events across diverse climatic regimes, while also prioritizing mechanistic analyses of how compound heatwave-drought interactions exacerbate glacier mass loss under projected climate warming.~~

This study integrated in situ glacio-meteorological observations from Sangqu Glacier with a surface energy–mass balance model to elucidate the mechanisms driving extreme glacier melt during the 2022 summer heatwave. To overcome the challenge of identifying extreme mass loss from short-term records, we developed a dual-threshold framework based on the mean and standard deviation. This approach effectively identifies extreme events in data-scarce regions, providing a robust diagnostic tool that circumvents the traditional requirement for decadal observational series.

Our findings reveal that the 2021/22 mass balance year experienced unprecedented mass loss. During the 2022 summer heatwave, glacier melt was 1.66 and 1.69 times higher than in the corresponding periods of 2019/20 and 2020/21, respectively, corresponding to an increase of 317.8 mm w.e.. This intensified melting was driven by synergistic anomalies in the surface energy balance, namely reduced albedo, enhanced downward longwave radiation, and increased sensible heat flux. These local-scale drivers were modulated by large-scale atmospheric circulation patterns, characterized by the westward expansion and intensification of the Western Pacific Subtropical High, the eastward extension of the South Asian High, and the poleward shift of the westerlies.

In summary, this study improves our understanding of glacier mass balance responses to extreme weather and climate events on the central Tibetan Plateau. The findings highlight the critical role of glacier surface energy balance anomalies in driving extreme melt during heatwaves and emphasize the importance of large-scale atmospheric circulation anomalies. This study has certain limitations, mainly including the limited spatial representativeness due to single-point meteorological observations and the omission of feedback effects from dynamic glacier geometry changes on mass balance. Future research should conduct detailed in situ observations of glacier surface micrometeorology, mass balance, and runoff across different climatic zones on the Tibetan Plateau to further elucidate the mechanisms of extreme melt during summer heatwaves and their impacts on hydrological processes, thereby providing a scientific basis for water resource management and hazard risk assessment.

Acknowledgements We thank the editor and anonymous reviewers for their constructive feedback on the manuscript, which led to substantial improvements during the review process.

Code and Data Availability Statement Meteorological data from the Tuotuohe meteorological station was obtained from the China Meteorological Administration's website (http://data.cma.cn/). ERA5 is available for download at https://cds.

climate.copernicus.eu/cdsapp#!/search?type=dataset. The EBFM model is available via https://github.com/ wardvp/EBFM-glacier. The Dual-Threshold Framework can be found at https://github.com/zhuzhufeifei/detect_extreme_events. Data supporting the findings of this study are available from the corresponding author upon reasonable request.

Author contribution All authors contributed to the study conception and design. Data collection was performed by F. Z. Analysis was performed by F. Z, M. Z and L. A. The first draft of the manuscript was written by F. Z and all authors commented on previous versions of the manuscript. All authors read and approved the final manuscript.

Competing interests: The authors declare that they have no conflict of interest.

Financial support This study is jointly funded by the Second Tibetan Plateau Scientific Expedition and Research Program (2024QZKK0400 and 2024QZKK0100), the Science and Technology Project of the Xizang Autonomous Region (XZ202501ZY0081 and XZ202501JD0025) and National Key Research and Development Project (2024YFF0808601).~~This study was jointly funded by the National Key R&D Program of China (Grant No. 2024YFF0808302, 2024YFF0808601), the Science and Technology Projects of Xizang Autonomous Region, China (Grant No. XZ202501JD0025), and Second TP Scientific Expedition and Research Program (Grant No. 2019QZKK0201).~~s

References

Anderson, S. and Radic, V.: Modeling the Streamflow Response to Heatwaves Across Glacierized Basins in Southwestern Canada, Water Resour. Res., 59, https://doi.org/10.1029/2023WR035428, 2023.

Bernard, É. and Friedt, J.-M.: Did a global heatwave have a lasting impact on the snowpack and the annual glacier mass balance? The example of a small glacial basin observatory in the High Arctic (Brøgger Peninsula, Spitsbergen), Arctic, Antarctic, and Alpine Research, 57, 2479899, https://doi.org/10.1080/15230430.2025.2479899, 2025.

Bhattacharya, A., Bolch, T., Mukherjee, K., King, O., Menounos, B., Kapitsa, V., Neckel, N., Yang, W., and Yao, T.: High Mountain Asian glacier response to climate revealed by multi-temporal satellite observations since the 1960s, Nat. Commun., 12, 4133, https://doi.org/10.1038/s41467-021-24180-y, 2021.

Bolch, T., Kulkarni, A., Kääb, A., Huggel, C., Paul, F., Cogley, J. G., Frey, H., Kargel, J. S., Fujita, K., Scheel, M., Bajracharya, S., and Stoffel, M.: The State and Fate of Himalayan Glaciers, Science, 336, 310–314, https://doi.org/10.1126/science.1215828, 2012.

Bolibar, J., Rabatel, A., Gouttevin, I., Zekollari, H., and Galiez, C.: Nonlinear sensitivity of glacier mass balance to future climate change unveiled by deep learning, Nat. Commun., 13, 409, https://doi.org/10.1038/s41467-022-28033-0, 2022.

Bougamont, M., Bamber, J. L., and Greuell, W.: A surface mass balance model for the Greenland Ice Sheet, J. Geophys. Res.: Earth Surf., 110, https://doi.org/10.1029/2005JF000348, 2005.

Boon, S., Sharp, M., and Nienow, P.: Impact of an extreme melt event on the runoff and hydrology of a high Arctic glacier, Hydrol. Processes, 17, 1051–1072, https://doi.org/10.1002/hyp.1194, 2003.

Brun, F., Berthier, E., Wagnon, P., Kääb, A., and Treichler, D.: A spatially resolved estimate of High Mountain Asia glacier mass balances from 2000 to 2016, Nat. Geosci., 10, 668–673, https://doi.org/10.1038/ngeo2999, 2017.

Brunt, D.: Notes on radiation in the atmosphere. I, Q. J. R. Meteorolog. Soc., 58, 389–420, https://doi.org/10.1002/qj.49705824704, 1932.

Chen, J., Xue, X., and Du, W.: Short communication: Extreme glacier mass loss triggered by high temperature and drought during hydrological year 2022 / 2023 in Qilian Mountains, Res. Cold Arid Reg., 16, 1–4, https://doi.org/10.1016/j.rcar.2024.01.002, 2024.

Cremona, A., Huss, M., Landmann, J. M., Borner, J., and Farinotti, D.: European heat waves 2022: contribution to extreme glacier melt in Switzerland inferred from automated ablation readings, Cryosphere, 17, 1895–1912, https://doi.org/10.5194/tc-17-1895-2023, 2023.

Draeger, C., Radić, V., White, R. H., and Tessema, M. A.: Evaluation of reanalysis data and dynamical downscaling for surface energy balance modeling at mountain glaciers in western Canada, Cryosphere, 18, 17–42, https://doi.org/10.5194/tc-18-17-2024, 2024.

Duan, J., Zhang, H., Jian, D., Xiao, C., Hao, F., Zhu, H., Lott, F. C., and Stott, P. A.: Influences of Anthropogenic Forcing on the Exceptionally Warm August 2022 over the Eastern Tibetan Plateau, Bull. Am. Meteorol. Soc., 105, E1068–E1073, https://doi.org/10.1175/BAMS-D-23-0179.1, 2024.

Duan, Q., Sorooshian, S., and Gupta, V.: Effective and efficient global optimization for conceptual rainfall-runoff models, Water Resour. Res., 28, 1015–1031, https://doi.org/10.1029/91WR02985, 1992.

Dussaillant, I., Hugonnet, R., Huss, M., Berthier, E., Bannwart, J., Paul, F., and Zemp, M.: Annual mass change of the world's glaciers from 1976 to 2024 by temporal downscaling of satellite data with in situ observations, Earth Syst. Sci. Data, 17, 1977–2006, https://doi.org/10.5194/essd-17-1977-2025, 2025.

Fujita, K., Seko, K., Ageta, Y., Jianchen, P., and Tandong, Y.: Superimposed ice in glacier mass balance on the Tibetan Plateau, J. Glaciol., 42, 454–460, https://doi.org/10.3189/S0022143000003440, 1996.

Gao, H., He, X., Ye, B., and Pu, J.: Modeling the runoff and glacier mass balance in a small watershed on the Central Tibetan Plateau, China, from 1955 to 2008, Hydrol. Processes, 26, 1593–1603, https://doi.org/10.1002/hyp.8256, 2012.

Guo, W., Liu, S., Xu, J., Wu, L., Shangguan, D., Yao, X., Wei, J., Bao, W., Yu, P., Liu, Q., and Jiang, Z.: The second Chinese glacier inventory: data, methods and results, J. Glaciol., 61, 357–372, https://doi.org/10.3189/2015JoG14J209, 2015.

Hock, R. and Holmgren, B.: A distributed surface energy-balance model for complex topography and its application to Storglaciären, Sweden, J. Glaciol., 51, 25–36, https://doi.org/10.3189/172756505781829566, 2005.

Hoffmann, L., Günther, G., Li, D., Stein, O., Wu, X., Griessbach, S., Heng, Y., Konopka, P., Müller, R., Vogel, B., and Wright, J. S.: From ERA-Interim to ERA5: the considerable impact of ECMWF's next-generation reanalysis on Lagrangian transport simulations, Atmos. Chem. Phys., 19, 3097–3124, https://doi.org/10.5194/acp-19-3097-2019, 2019.

Hua, W., Dai, A., Qin, M., Hu, Y., and Cui, Y.: How Unexpected Was the 2022 Summertime Heat Extremes in the Middle Reaches of the Yangtze River?, Geophys. Res. Lett., 50, e2023GL104269, https://doi.org/10.1029/2023GL104269, 2023.

Hugonnet, R., McNabb, R., Berthier, E., Menounos, B., Nuth, C., Girod, L., Farinotti, D., Huss, M., Dussaillant, I., Brun, F., and Kääb, A.: Accelerated global glacier mass loss in the early twenty-first century, Nature, 592, 726–731, https://doi.org/10.1038/s41586-021-03436-z, 2021.

Izagirre, E., Revuelto, J., Vidaller, I., Deschamps-Berger, C., Rojas-Heredia, F., Rico, I., Alonso-González, E., Gascoin, S., Serrano, E., and López-Moreno, J. I.: Pyrenean glaciers are disappearing fast: state of the glaciers after the extreme mass losses in 2022 and 2023, Reg Environ Change, 24, 172, https://doi.org/10.1007/s10113-024-02333-1, 2024.

Jeong, H., Park, H.-S., Chowdary, J. S., and Xie, S.-P.: Triple-Dip La Niña Contributes to Pakistan Flooding and Southern China Drought in Summer 2022, Bull. Am. Meteorol. Soc., 104, E1570–E1586, https://doi.org/10.1175/BAMS-D-23-0002.1, 2023.

Jiang, J., Liu, Y., Meng, J., Wu, G., He, B., Ma, T., Bao, W., and Fan, J.: Dry soil moisture on the Tibetan Plateau drives synchronous extreme heatwaves in Europe and east Asia, npj Clim. Atmos. Sci., 7, 281–290, https://doi.org/10.1038/s41612-024-00831-x, 2024.

K. Deb, A. Pratap, S. Agarwal, and T. Meyarivan: A fast and elitist multiobjective genetic algorithm: NSGA-II, IEEE Trans. Evol. Comput., 6, 182–197, https://doi.org/10.1109/4235.996017, 2002.

Kang, S., Wang, F., Morgenstern, U., Zhang, Y., Grigholm, B., Kaspari, S., Schwikowski, M., Ren, J., Yao, T., Qin, D., and Mayewski, P. A.: Dramatic loss of glacier accumulation area on the Tibetan Plateau revealed by ice core tritium and mercury records, Cryosphere, 9, 1213–1222, https://doi.org/10.5194/tc-9-1213-2015, 2015.

King, O., Ghuffar, S., Bhattacharya, A., Yao, R., Yao, T., and Bolch, T.: Glaciological and climatological drivers of heterogeneous glacier mass loss in the Tanggula Shan (Central-Eastern Tibetan Plateau), since the 1960s, J. Glaciol., 69, 1149–1166, https://doi.org/10.1017/jog.2023.5, 2023.

Kinnard, C., Larouche, O., Demuth, M. N., and Menounos, B.: Modelling glacier mass balance and climate sensitivity in the context of sparse observations: application to Saskatchewan Glacier, western Canada, Cryosphere, 16, 3071–3099, https://doi.org/10.5194/tc-16-3071-2022, 2022.

Koboltschnig, G. R., Schöner, W., Holzmann, H., and Zappa, M.: Glaciermelt of a small basin contributing to runoff under the extreme climate conditions in the summer of 2003, Hydrol. Processes, 23, 1010–1018, https://doi.org/10.1002/hyp.7203, 2009.

Koboltschnig, G. R. and Schöner, W.: The relevance of glacier melt in the water cycle of the Alps: the example of Austria, Hydrol. Earth Syst. Sci., 15, 2039–2048, https://doi.org/10.5194/hess-15-2039-2011, 2011.

Kondo, K., Sugiyama, S., Sakakibara, D., and Fukumoto, S.: Flood events caused by discharge from Qaanaaq Glacier, northwestern Greenland, J. Glaciol., 67, 500–510, https://doi.org/10.1017/jog.2021.3, 2021.

Kronenberg, M., Van Pelt, W., Machguth, H., Fiddes, J., Hoelzle, M., and Pertziger, F.: Long-term firn and mass balance modelling for Abramov Glacier in the data-scarce Pamir Alay, Cryosphere, 16, 5001–5022, https://doi.org/10.5194/tc-16-5001-2022, 2022.

Li, Z., Xiao, Z., and Ling, J.: Impact of extremely warm Tibetan Plateau in spring on the rare rainfall anomaly pattern in the regions west and east to Plateau in late summer 2022, Atmos. Res., 290, 106797, https://doi.org/10.1016/j.atmosres.2023.106797, 2023.

Liang, L., Cuo, L., and Liu, Q.: The energy and mass balance of a continental glacier: Dongkemadi Glacier in central Tibetan Plateau, Sci. Rep., 8, 12788, https://doi.org/10.1038/s41598-018-31228-5, 2018.

(Lisette) Klok, E. J. and Oerlemans, J.: Model study of the spatial distribution of the energy and mass balance of Morteratschgletscher, Switzerland, J. Glaciol., 48, 505–518, https://doi.org/10.3189/172756502781831133, 2002.

Liu, W., Zhang, D., Qin, X., Van Den Broeke, M. R., Jiang, Y., Yang, D., and Ding, M.: Monsoon Clouds Control the Summer Surface Energy Balance on East Rongbuk Glacier (6,523 m Above Sea Level), the Northern of Mt. Qomolangma (Everest), J. Geophys. Res.: Atmos., 126, e2020JD033998, https://doi.org/10.1029/2020JD033998, 2021.

Menounos, B., Huss, M., Marshall, S., Ednie, M., Florentine, C., and Hartl, L.: Glaciers in Western Canada-Conterminous US and Switzerland Experience Unprecedented Mass Loss Over the Last Four Years (2021–2024), Geophys. Res. Lett., 52, e2025GL115235, https://doi.org/10.1029/2025GL115235, 2025.

Mölg, T., Cullen, N. J., Hardy, D. R., Kaser, G., and Klok, L.: Mass balance of a slope glacier on Kilimanjaro and its sensitivity to climate, Int. J. Climatol., 28, 881–892, https://doi.org/10.1002/joc.1589, 2008.

Oerlemans, J. and Knap, W. H.: A 1 year record of global radiation and albedo in the ablation zone of Morteratschgletscher, Switzerland, J. Glaciol., 44, 231–238, https://doi.org/10.3189/S0022143000002574, 1998.

Oerlemans, J., Anderson, B., Hubbard, A., Huybrechts, Ph., Jóhannesson, T., Knap, W. H., Schmeits, M., Stroeven, A. P., Van De Wal, R. S. W., Wallinga, J., and Zuo, Z.: Modelling the response of glaciers to climate warming, Clim. Dyn., 14, 267–274, https://doi.org/10.1007/s003820050222, 1998.

Östin, R. and Andersson, S.: Frost growth parameters in a forced air stream, Int. J. Heat Mass Transfer, 34, 1009–1017, https://doi.org/10.1016/0017-9310(91)90012-4, 1991.

Pu, J., Yao, T., Yang, M., Tian, L., Wang, N., Ageta, Y., and Fujita, K.: Rapid decrease of mass balance observed in the Xiao (Lesser) Dongkemadi Glacier, in the central Tibetan Plateau, Hydrol. Processes, 22, 2953–2958, https://doi.org/10.1002/hyp.6865, 2008.

Raei, E., Nikoo, M. R., AghaKouchak, A., Mazdiyasni, O., and Sadegh, M.: GHWR, a multi-method global heatwave and warm-spell record and toolbox, Sci. Data, 5, 180206, https://doi.org/10.1038/sdata.2018.206, 2018.

Reijmer, C. H. and Hock, R.: Internal accumulation on Storglaciären, Sweden, in a multi-layer snow model coupled to a distributed energy- and mass-balance model, J. Glaciol., 54, 61–72, https://doi.org/10.3189/002214308784409161, 2008.

Shan, B., Verhoest, N. E. C., and De Baets, B.: Identification of compound drought and heatwave events on a daily scale and across four seasons, Hydrol. Earth Syst. Sci., 28, 2065–2080, https://doi.org/10.5194/hess-28-2065-2024, 2024.

Sturm, M., Holmgren, J., König, M., and Morris, K.: The thermal conductivity of seasonal snow, J. Glaciol., 43, 26–41, https://doi.org/10.3189/S0022143000002781, 1997.

Thibert, E., Dkengne Sielenou, P., Vionnet, V., Eckert, N., and Vincent, C.: Causes of Glacier Melt Extremes in the Alps Since 1949, Geophys. Res. Lett., 45, 817–825, https://doi.org/10.1002/2017GL076333, 2018.

Tian, L., Masson-Delmotte, V., Stievenard, M., Yao, T., and Jouzel, J.: Tibetan Plateau summer monsoon northward extent revealed by measurements of water stable isotopes, J. Geophys. Res.: Atmos., 106, 28081–28088, https://doi.org/10.1029/2001JD900186, 2001.

Tian, Y., Ghausi, S. A., Zhang, Y., Zhang, M., Xie, D., Cao, Y., Mei, Y., Wang, G., Zhong, D., and Kleidon, A.: Radiation as the dominant cause of high-temperature extremes on the eastern Tibetan Plateau, Environ. Res. Lett., 18, 074007, https://doi.org/10.1088/1748-9326/acd805, 2023.

Van Tiel, M., Huss, M., Zappa, M., Jonas, T., and Farinotti, D.: Swiss glacier mass loss during the 2022 drought: persistent streamflow contributions amid declining melt water volumes, Hydrol, Earth Syst, Sci, 30, 23–43, https://doi.org/10.5194/hess-30-23-2026, 2026.

Van Pelt, W., Pohjola, V., Pettersson, R., Marchenko, S., Kohler, J., Luks, B., Hagen, J. O., Schuler, T. V., Dunse, T., Noël, B., and Reijmer, C.: A long-term dataset of climatic mass balance, snow conditions, and runoff in Svalbard (1957–2018), Cryosphere, 13, 2259–2280, https://doi.org/10.5194/tc-13-2259-2019, 2019.

Van Pelt, W. J. J., Oerlemans, J., Reijmer, C. H., Pohjola, V. A., Pettersson, R., and Van Angelen, J. H.: Simulating melt, runoff and refreezing on Nordenskiöldbreen, Svalbard, using a coupled snow and energy balance model, Cryosphere, 6, 641–659, https://doi.org/10.5194/tc-6-641-2012, 2012.

Vargo, L. J., Anderson, B. M., Dadić, R., Horgan, H. J., Mackintosh, A. N., King, A. D., and Lorrey, A. M.: Anthropogenic warming forces extreme annual glacier mass loss, Nat. Clim. Change, 10, 856–861, https://doi.org/10.1038/s41558-020-0849-2, 2020.

Voordendag, A., Prinz, R., Schuster, L., and Kaser, G.: Brief communication: The Glacier Loss Day as an indicator of a record-breaking negative glacier mass balance in 2022, Cryosphere, 17, 3661–3665, https://doi.org/10.5194/tc-17-3661-2023, 2023.

Wang, Z., Duan, A., Yang, S., and Ullah, K.: Atmospheric moisture budget and its regulation on the variability of summer precipitation over the Tibetan Plateau, J. Geophys. Res.: Atmos., 122, 614–630, https://doi.org/10.1002/2016JD025515, 2017.

Wei, Y. and Yu, H.: The Interdecadal Weakening of the Relationship Between Indian Ocean Sea Surface Temperature and Summer Precipitation in Central Asia, Geophys. Res. Lett., 51, e2023GL107371, https://doi.org/10.1029/2023GL107371, 2024.

Xu, C., Li, H., Wang, F., Li, Z., Zhou, P., and Liu, S.: Heatwaves in summer 2022 forces substantial mass loss for Urumqi Glacier No. 1, China, J. Glaciol., 70, e77, https://doi.org/10.1017/jog.2024.4, 2024.

Yan, R., Wang, X., Wang, J., Tan, J., and Ju, W.: Warm Early Summer Compensated Reduction in Photosynthesis Caused by 2022 Late Summer Extreme Drought Over the Tibetan Plateau, J. Geophys. Res.: Biogeosci., 129, e2023JG007859, https://doi.org/10.1029/2023JG007859, 2024.

Yao, T., Thompson, L., Yang, W., Yu, W., Gao, Y., Guo, X., Yang, X., Duan, K., Zhao, H., Xu, B., Pu, J., Lu, A., Xiang, Y., Kattel, D. B., and Joswiak, D.: Different glacier status with atmospheric circulations in Tibetan Plateau and surroundings, Nat. Clim. Change, 2, 663–667, https://doi.org/10.1038/nclimate1580, 2012.

Yao, T., Masson-Delmotte, V., Gao, J., Yu, W., Yang, X., Risi, C., Sturm, C., Werner, M., Zhao, H., He, Y., Ren, W., Tian, L., Shi, C., and Hou, S.: A review of climatic controls on δ^{18} O in precipitation over the Tibetan Plateau: Observations and simulations, Rev. Geophys., 51, 525–548, https://doi.org/10.1002/rog.20023, 2013.

Yao, T., Bolch, T., Chen, D., Gao, J., Immerzeel, W., Piao, S., Su, F., Thompson, L., Wada, Y., Wang, L., Wang, T., Wu, G., Xu, B., Yang, W., Zhang, G., and Zhao, P.: The imbalance of the Asian water tower, Nat. Rev. Earth Environ., 3, 618–632, https://doi.org/10.1038/s43017-022-00299-4, 2022.

Yen, Y.: Review of thermal properties of snow, ice and sea ice, Tech. rep., DTIC Document, 1981.

Zhang, T., Deng, Y., Chen, J., Yang, S., and Dai, Y.: An energetics tale of the 2022 mega-heatwave over central-eastern China, npj Clim. Atmos. Sci., 6, 162, https://doi.org/10.1038/s41612-023-00490-4, 2023.

Zhou, B., Zhai, P., and Liao, Z.: Bivariate attribution of the compound hot and dry summer of 2022 on the Tibetan Plateau, Sci. China Earth Sci., 67, 2122–2136, https://doi.org/10.1007/s11430-023-1320-y, 2024.

Zhu, F., Zhu, M., Yang, W., Wang, Z., Guo, Y., and Yao, T.: Drivers of the Extreme Early Spring Glacier Melt of 2022 on the Central Tibetan Plateau, Earth Space Sci., 11, https://doi.org/10.1029/2023ea003297, 2024a.

Zhu, F., Zhu, M., Guo, Y., and Yao, T.: Observation and Simulation of Runoff During an Extreme Heatwave in a Glacial Basin on the Central Tibetan Plateau, Hydrol. Processes, 38, e70014, https://doi.org/10.1002/hyp.70014, 2024b.

Zhu, F., Yao, T.-D., Zhu, M.-L., An, L., Wang, P., Huang, G.-F., and Hu, Z.-F.: The role of mid-latitude zonal wind anomalies in extreme glacier mass loss on central Tibetan Plateau, Adv. Clim. Change Res., https://doi.org/10.1016/j.accre.2026.03.010, 2026a.

Zhu, M., Yao, T., Yang, W., Xu, B., Wu, G., and Wang, X.: Differences in mass balance behavior for three glaciers from different climatic regions on the Tibetan Plateau, Clim. Dyn., 50, 3457–3484, https://doi.org/10.1007/s00382-017-3817-4, 2018.

Zhu, M., Thompson, L. G., Zhao, H., Yao, T., Yang, W., and Jin, S.: Influence of atmospheric circulation on glacier mass balance in western Tibet: an analysis based on observations and modeling, J. Clim., 1–55, https://doi.org/10.1175/JCLI-D-20-0988.1, 2021.

Zhu, M., Yao, T., Thompson, L. G., Wang, S., Yang, W., and Zhao, H.: What induces the spatiotemporal variability of glacier mass balance across the Qilian Mountains, Clim Dyn, 59, 3555–3577, https://doi.org/10.1007/s00382-022-06283-4, 2022a.

Zhu, M., Yao, T., Yang, W., Wu, G., Li, S., Zhao, H., and Thompson, L. G.: Possible Causes of Anomalous Glacier Mass Balance in the Western Kunlun Mountains, J. Geophys. Res.: Atmos., 127, e2021JD035705, https://doi.org/10.1029/2021JD035705, 2022b.

Zhu, M., Yao, T., Thompson, L. G., Yang, W., Zhu, F., Lin, D., Zhong, Z.-P., Zhao, H., Zhang, X., and Li, S.: Linking northeastern indian subcontinental high temperature to extreme glacier mass loss on the south-central Tibetan Plateau, J. Geophys. Res.: Atmos., 131, e2025JD045031, https://doi.org/10.1029/2025JD045031, 2026b.

Anderson, S., & Radic, V. (2023). Modeling the Streamflow Response to Heatwaves Across Glacierized Basins in Southwestern Canada. *WATER RESOURCES RESEARCH*, *59*(12). https://doi.org/10.1029/2023WR035428

Beckmann J, Winkelmann R (2023) Effects of extreme melt events on ice flow and sea level rise of the Greenland Ice Sheet. The Cryosphere 17:3083–3099. https://doi.org/10.5194/tc-17-3083-2023

Bolch T, Kulkarni A, Kääb A, et al (2012) The State and Fate of Himalayan Glaciers. Science 336:310–314. https://doi.org/10.1126/science.1215828

Bougamont M, Bamber JL, Greuell W (2005) A surface mass balance model for the Greenland Ice Sheet. J Geophys Res 110:2005JF000348. https://doi.org/10.1029/2005JF000348

Brun F, Berthier E, Wagnon P, et al (2017) A spatially resolved estimate of High Mountain Asia glacier mass balances from 2000 to 2016. Nature Geosci 10:668–673. https://doi.org/10.1038/ngeo2999

Brunt D (1932) Notes on radiation in the atmosphere. I. Quart J Royal Meteoro Soc 58:389–420. https://doi.org/10.1002/qj.49705824704

Chen J, Xue X, Du W (2024) Short communication: Extreme glacier mass loss triggered by high temperature and drought during hydrological year 2022 / 2023 in Qilian Mountains. Research in Cold and Arid Regions 16:1–4. https://doi.org/10.1016/j.rcar.2024.01.002

Chen R, Li X (2023) Causes of the persistent merging of the western North Pacific subtropical high and the Iran high during late July 2022. Clim Dyn 61:2285–2297. https://doi.org/10.1007/s00382-023-06678-x

Duan J, Zhang H, Jian D, et al (2024) Influences of Anthropogenic Forcing on the Exceptionally Warm August 2022 over the Eastern Tibetan Plateau. Bulletin of the American Meteorological Society 105:E1068–E1073. https://doi.org/10.1175/BAMS-D-23-0179.1

Favier V, Wagnon P, Chazarin J, et al (2004) One-year measurements of surface heat budget on the ablation zone of Antizana Glacier 15, Ecuadorian Andes. J Geophys Res 109:2003JD004359. https://doi.org/10.1029/2003JD004359

Guo S, Chen R, Li H (2022) Surface Sublimation/Evaporation and Condensation/Deposition and Their Links to Westerlies During 2020 on the August-One Glacier, the Semi-Arid Qilian Mountains of Northeast Tibetan Plateau. JGR Atmospheres 127:e2022JD036494. https://doi.org/10.1029/2022JD036494

Guo W, Liu S, Xu J, et al (2015) The second Chinese glacier inventory: data, methods and results. J Glaciol 61:357–372. https://doi.org/10.3189/2015JoG14J209

Hock R, Holmgren B (2005) A distributed surface energy-balance model for complex topography and its application to Storglaciären, Sweden. J Glaciol 51:25–36. https://doi.org/10.3189/172756505781829566

Hoffmann L, Günther G, Li D, et al (2019) From ERA-Interim to ERA5: the considerable impact of ECMWF's next-generation reanalysis on Lagrangian transport simulations. Atmos Chem Phys 19:3097–3124. https://doi.org/10.5194/acp-19-3097-2019

Hua W, Dai A, Qin M, et al (2023) How Unexpected Was the 2022 Summertime Heat Extremes in the Middle Reaches of the Yangtze River? Geophysical Research Letters 50:e2023GL104269. https://doi.org/10.1029/2023GL104269

Hugonnet R, McNabb R, Berthier E, et al (2021) Accelerated global glacier mass loss in the early twenty-first century. Nature 592:726–731. https://doi.org/10.1038/s41586-021-03436-z

Immerzeel WW, Lutz AF, Andrade M, et al (2020) Importance and vulnerability of the world's water towers. Nature 577:364–369. https://doi.org/10.1038/s41586-019-1822-y

Jeong H, Park H-S, Chowdary JS, Xie S-P (2023) Triple-Dip La Niña Contributes to Pakistan Flooding and Southern China Drought in Summer 2022. Bulletin of the American Meteorological Society 104:E1570–E1586. https://doi.org/10.1175/BAMS-D-23-0002.1

Kang S, Wang F, Morgenstern U, et al (2015) Dramatic loss of glacier accumulation area on the Tibetan Plateau revealed by ice core tritium and mercury records. The Cryosphere 9:1213–1222. https://doi.org/10.5194/tc-9-1213-2015

King O, Ghuffar S, Bhattacharya A, et al (2023) Glaciological and climatological drivers of heterogeneous glacier mass loss in the Tanggula Shan (Central-Eastern Tibetan Plateau), since the 1960s. J Glaciol 69:1149–1166. https://doi.org/10.1017/jog.2023.5

Kronenberg M, Van Pelt W, Machguth H, et al (2022) Long-term firn and mass balance modelling for Abramov Glacier in the data-scarce Pamir Alay. The Cryosphere 16:5001–5022. https://doi.org/10.5194/tc-16-5001-2022

Li N, Xiao Z, Zhao L (2021) A Recent Increase in Long-Lived Heatwaves in China Under the Joint Influence of South Asia and Western North Pacific Subtropical Highs. Journal of Climate 1–42. https://doi.org/10.1175/JCLI-D-21-0014.1

Li S, Yao T, Yang W, et al (2018) Glacier Energy and Mass Balance in the Inland Tibetan Plateau: Seasonal and Interannual Variability in Relation to Atmospheric Changes. JGR Atmospheres 123:6390–6409. https://doi.org/10.1029/2017JD028120

Li Z, Xiao Z, Ling J (2023) Impact of extremely warm Tibetan Plateau in spring on the rare rainfall anomaly pattern in the regions west and east to Plateau in late summer 2022. Atmospheric Research 290:106797. https://doi.org/10.1016/j.atmosres.2023.106797

Liang L, Cuo L, Liu Q (2019) Mass Balance Variation and Associative Climate Drivers for the Dongkemadi Glacier in the Central Tibetan Plateau. JGR Atmospheres 124:10814–10825. https://doi.org/10.1029/2019JD030615

(Lisette) Klok EJ, Oerlemans J (2002) Model study of the spatial distribution of the energy and mass balance of Morteratschgletscher, Switzerland. J Glaciol 48:505–518. https://doi.org/10.3189/172756502781831133

Liu W, Zhang D, Qin X, et al (2021) Monsoon Clouds Control the Summer Surface Energy Balance on East Rongbuk Glacier (6,523 m Above Sea Level), the Northern of Mt. Qomolangma (Everest). JGR Atmospheres 126:e2020JD033998. https://doi.org/10.1029/2020JD033998

Mölg T, Cullen NJ, Hardy DR, et al (2008) Mass balance of a slope glacier on Kilimanjaro and its sensitivity to climate. Intl Journal of Climatology 28:881–892. https://doi.org/10.1002/joc.1589

Oerlemans J, Knap WH (1998) A 1 year record of global radiation and albedo in the ablation zone of Morteratschgletscher, Switzerland. J Glaciol 44:231–238. https://doi.org/10.3189/S0022143000002574

Potocki M, Mayewski PA, Matthews T, et al (2022) Mt. Everest's highest glacier is a sentinel for accelerating ice loss. npj Clim Atmos Sci 5:7. https://doi.org/10.1038/s41612-022-00230-0

Pu J, Yao T, Yang M, et al (2008) Rapid decrease of mass balance observed in the Xiao (Lesser) Dongkemadi Glacier, in the central Tibetan Plateau. Hydrological Processes 22:2953–2958. https://doi.org/10.1002/hyp.6865

Raei E, Nikoo MR, AghaKouchak A, et al (2018) GHWR, a multi-method global heatwave and warm-spell record and toolbox. Sci Data 5:180206. https://doi.org/10.1038/sdata.2018.206

Reijmer CH, Hock R (2008) Internal accumulation on Storglaciären, Sweden, in a multi-layer snow model coupled to a distributed energy- and mass-balance model. J Glaciol 54:61–72. https://doi.org/10.3189/002214308784409161

Shan B, Verhoest NEC, De Baets B (2024) Identification of compound drought and heatwave events on a daily scale and across four seasons. Hydrol Earth Syst Sci 28:2065–2080. https://doi.org/10.5194/hess-28-2065-2024

Thibert E, Dkengne Sielenou P, Vionnet V, et al (2018) Causes of Glacier Melt Extremes in the Alps Since 1949. Geophysical Research Letters 45:817–825. https://doi.org/10.1002/2017GL076333

Tian L, Masson-Delmotte V, Stievenard M, et al (2001) Tibetan Plateau summer monsoon northward extent revealed by measurements of water stable isotopes. J Geophys Res 106:28081–28088. https://doi.org/10.1029/2001JD900186

Tian Y, Ghausi SA, Zhang Y, et al (2023) Radiation as the dominant cause of high-temperature extremes on the eastern Tibetan Plateau. Environ Res Lett 18:074007. https://doi.org/10.1088/1748-9326/acd805

Van Pelt W, Pohjola V, Pettersson R, et al (2019) A long-term dataset of climatic mass balance, snow conditions, and runoff in Svalbard (1957–2018). The Cryosphere 13:2259–2280. https://doi.org/10.5194/tc-13-2259-2019

Van Pelt WJJ, Oerlemans J, Reijmer CH, et al (2012) Simulating melt, runoff and refreezing on Nordenskiöldbreen, Svalbard, using a coupled snow and energy balance model. The Cryosphere 6:641–659. https://doi.org/10.5194/tc-6-641-2012

Vargo, L. J., Anderson, B. M., Dadić, R., Horgan, H. J., Mackintosh, A. N., King, A. D., & Lorrey, A. M. (2020). Anthropogenic warming forces extreme annual glacier mass loss. Nature Climate Change, 10(9), 856–861. https://doi.org/10.1038/s41558-020-0849-2

Wei Lele, He Xiaobo, Xue Yu'ang, Wang Shaoyong, Guo Haonan, Ding Yongjian, & Yao Tandong. (2025). Analysis of the characteristics of Xiao Dongkemadi Glacier mass balance changes in Tanggula Mountains from 2005 to 2023. *Journal of Glaciology and Geocryology*, *47*(2), 317–329.

Xu C, Li H, Wang F, et al (2024) Heatwaves in summer 2022 forces substantial mass loss for Urumqi Glacier No. 1, China. Journal of Glaciology 70:e77. https://doi.org/10.1017/jog.2024.4

Yan R, Wang X, Wang J, et al (2024) Warm Early Summer Compensated Reduction in Photosynthesis Caused by 2022 Late Summer Extreme Drought Over the Tibetan Plateau. Journal of Geophysical Research: Biogeosciences 129:e2023JG007859. https://doi.org/10.1029/2023JG007859

Yang W, Yao T, Guo X, et al (2013) Mass balance of a maritime glacier on the southeast Tibetan Plateau and its climatic sensitivity. JGR Atmospheres 118:9579–9594. https://doi.org/10.1002/jgrd.50760

Yao T, Bolch T, Chen D, et al (2022) The imbalance of the Asian water tower. Nat Rev Earth Environ 3:618–632. https://doi.org/10.1038/s43017-022-00299-4

Yao T, Masson-Delmotte V, Gao J, et al (2013) A review of climatic controls on δ^{18}O in precipitation over the Tibetan Plateau: Observations and simulations. Reviews of Geophysics 51:525–548. https://doi.org/10.1002/rog.20023

Yao T, Thompson L, Yang W, et al (2012) Different glacier status with atmospheric circulations in Tibetan Plateau and surroundings. Nature Clim Change 2:663–667. https://doi.org/10.1038/nclimate1580

You Q, Wu F, Shen L, et al (2020) Tibetan Plateau amplification of climate extremes under global warming of 1.5 °C, 2 °C and 3 °C. Global and Planetary Change 192:103261. https://doi.org/10.1016/j.gloplacha.2020.103261

Zhang T, Deng Y, Chen J, et al (2023a) An energetics tale of the 2022 mega-heatwave over central-eastern China. npj Clim Atmos Sci 6:162. https://doi.org/10.1038/s41612-023-00490-4

Zhang T, Wang W, An B, Wei L (2023b) Enhanced glacial lake activity threatens numerous communities and infrastructure in the Third Pole. Nat Commun 14:8250. https://doi.org/10.1038/s41467-023-44123-z

Zhang J, Chen H, Fang X, et al (2024) Warming-induced hydrothermal anomaly over the Earth's three Poles amplifies concurrent extremes in 2022. npj Clim Atmos Sci 7:8. https://doi.org/10.1038/s41612-023-00553-6

Zhou B, Zhai P, Liao Z (2024) Bivariate attribution of the compound hot and dry summer of 2022 on the Tibetan Plateau. Sci China Earth Sci 67:2122–2136. https://doi.org/10.1007/s11430-023-1320-y

Zhu F, Zhu M, Guo Y, Yao T (2024a) Observation and Simulation of Runoff During an Extreme Heatwave in a Glacial Basin on the Central Tibetan Plateau. Hydrological Processes 38:e70014. https://doi.org/10.1002/hyp.70014

Zhu F, Zhu M, Yang W, et al (2024b) Drivers of the Extreme Early Spring Glacier Melt of 2022 on the Central Tibetan Plateau. Earth and Space Science 11:e2023EA003297. https://doi.org/10.1029/2023EA003297

Zhu M, Thompson LG, Yao T, et al (2023) Opposite mass balance variations between glaciers in western Tibet and the western Tien Shan. Global and Planetary Change 220:103997. https://doi.org/10.1016/j.gloplacha.2022.103997

Zhu M, Thompson LG, Zhao H, et al (2021) Influence of atmospheric circulation on glacier mass balance in western Tibet: an analysis based on observations and modeling. Journal of Climate 1–55. https://doi.org/10.1175/JCLI-D-20-0988.1

Zhu M, Yao T, Xie Y, et al (2020) Mass balance of Muji Glacier, northeastern Pamir, and its controlling climate factors. Journal of Hydrology 590:125447. https://doi.org/10.1016/j.jhydrol.2020.125447

Zhu M, Yao T, Yang W, et al (2018) Differences in mass balance behavior for three glaciers from different climatic regions on the Tibetan Plateau. Clim Dyn 50:3457–3484. https://doi.org/10.1007/s00382-017-3817-4

Zhu, M., Yao, T., Thompson, L. G., Wang, S., Yang, W., & Zhao, H. (2022a). What induces the spatiotemporal variability of glacier mass balance across the Qilian Mountains. *Climate Dynamics*, *59*(11–12), 3555–3577. https://doi.org/10.1007/s00382-022-06283-4

Zhu M, Yao T, Yang W, et al (2022b) Possible Causes of Anomalous Glacier Mass Balance in the Western Kunlun Mountains. JGR Atmospheres 127:e2021JD035705. https://doi.org/10.1029/2021JD035705

Appendix

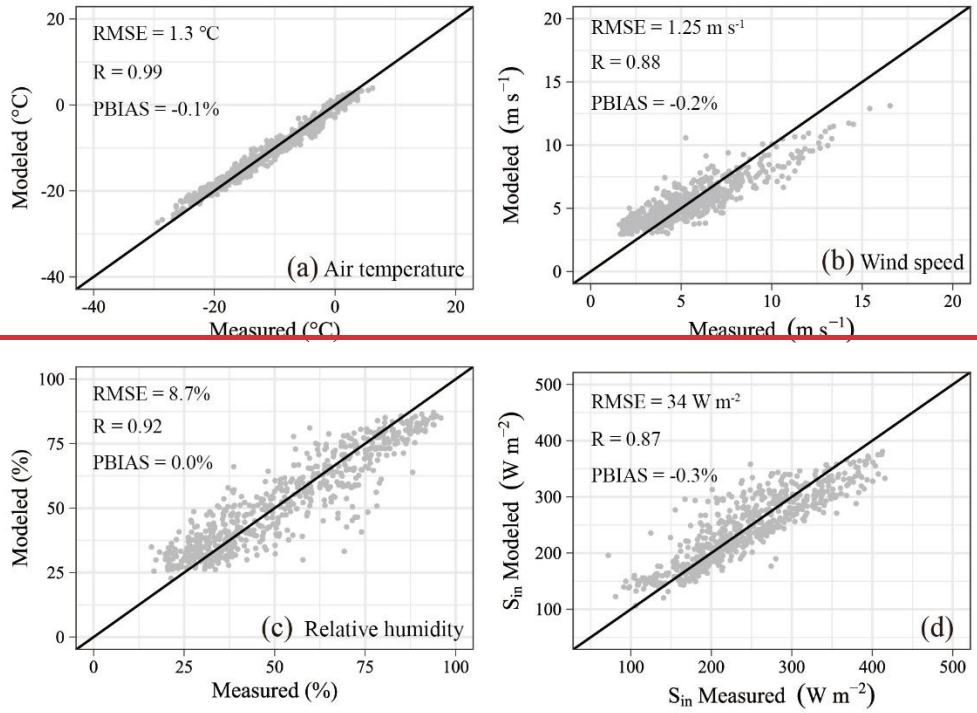


Figure A1. Comparison of observed and ERA5-downscaled (a) Air temperature, (b) Relative humidity, (c) Wind speed, and (d) Incoming shortwave radiation at the daily scale.

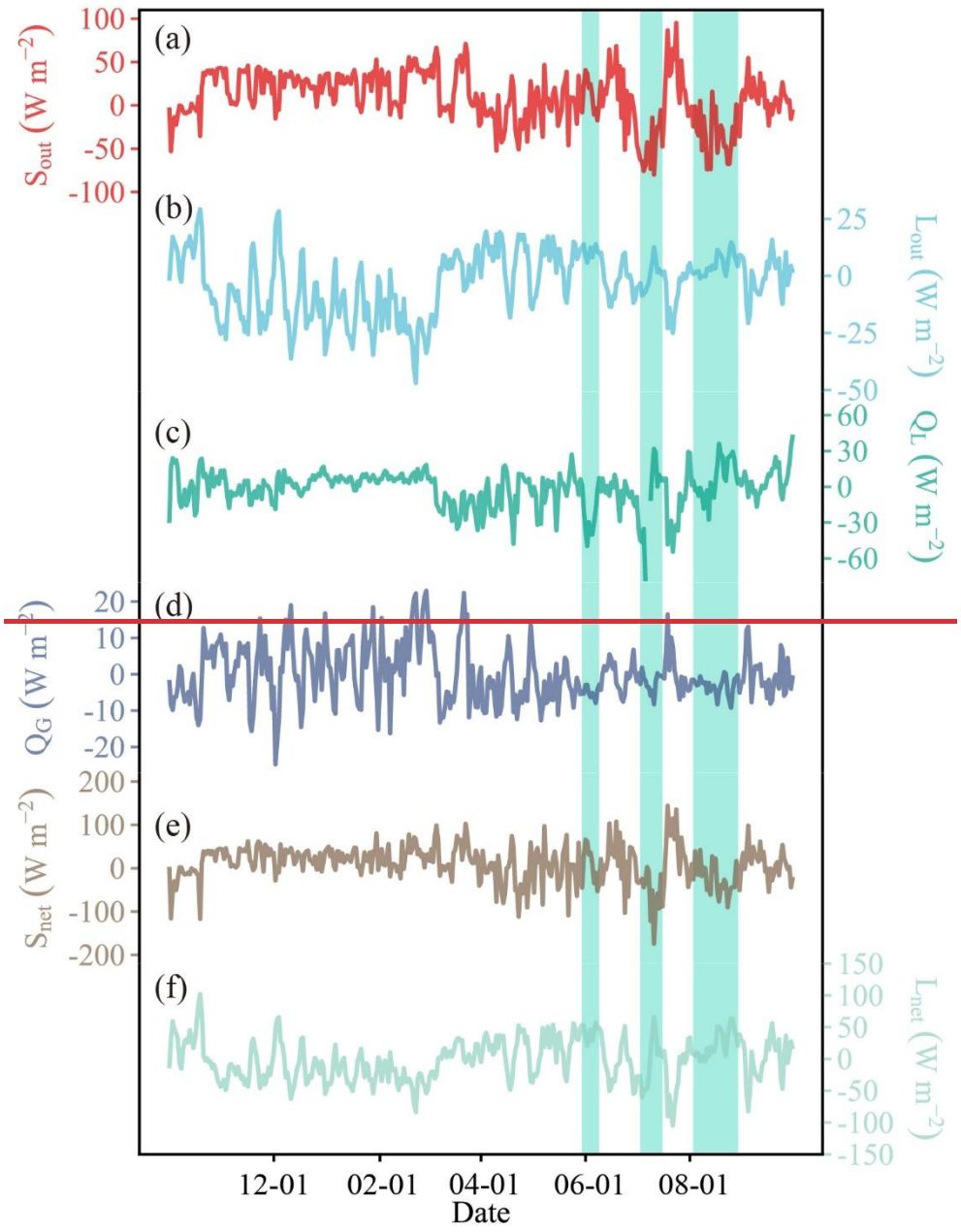


Figure A2. Energy balance components associated with the glacier melt events in summer 2022. Anomalous (a) Outgoing shortwave radiation, (b) Outgoing longwave radiation, (c) Latent heat fluxes, (d) Snow and ice heat flux, (e) Net shortwave radiation, and (f) Net longwave radiation from October 2021 to October 2022 (reference period is October 2019–September 2021). Color shading represents extreme heat waves.